Impacts of annealing temperature and time on the thermoelectric performance of recycled carbon fiber (RCF)/n-Bi2Te3 heterostructure thermoelectric composites.

JAGADISH, P., KHALID, M., WONG, W.P., PHEI LI. L., CHELVANATHAN, P., WALVEKAR, R., MUBARAK, N.M. and CHAN, A.

2023

Impacts of Annealing Temperature and Time on the Thermoelectric Performance of Recycled Carbon Fiber (RCF)/n-Bi2Te3 Heterostructure Thermoelectric Composites

Journal:	*ECS Journal of Solid State Science and Technology*
Manuscript ID	JSS-103601.R1
Manuscript Type:	Research Paper
Date Submitted by the Author:	05-Jun-2023

Complete List of Authors:	Jagadish, Priyanka; Sunway University Khalid, Mohammad ; Sunway University, Graphene and Advanced 2D Materials Research Group Wong, Weng Pin; Sunway University Phei Li, Lau; University of Nottingham Malaysia Chelvanathan, Puvaneswaran ; UKM Walvekar, Rashmi.; Xiamen University - Malaysia, Department of Chemical Engineering, School of Energy and Chemical Engineering Nabisab Mujawar, Mubarak; University of Technology Brunei Chan, Andy; Robert Gordon University

Keywords:	Thermoelectric, Bismuth telluride (Bi2Te3), Annealing, Recycled carbon fibre (RCF), Seebeck coefficient

Impacts of Annealing Temperature and Time on the Thermoelectric Performance of Recycled Carbon Fiber (RCF)/n-Bi_2Te_3 Heterostructure Thermoelectric Composites

Priyanka R. Jagadish,[1] Mohammad Khalid,[1,2,3,z] Wong Weng Pin,[1] Lau Phei Li,[4] Puvaneswaran Chelvanathan,[1,5] Rashmi Walvekar,[6] N. M. Mubarak,[7] and Andy Chan[8]

[1]Graphene & Advanced 2D Materials Research Group (GAMRG), School of Engineering and Technology, Sunway University, Bandar Sunway, 47500 Petaling Jaya, Selangor, Malaysia
[2]Uttaranchal University, Dehradun, 248007 Uttarakhand, India
[3]Division of Research & Development, Lovely Professional University, Phagwara, Punjab 144411, India
[4]Department of Chemical and Environmental Engineering, Faculty of Engineering, University of Nottingham Malaysia, 43500, Semenyih, Selangor, Malaysia
[5]Solar Energy Research Institute (SERI), Universiti Kebangsaan Malaysia (UKM), 43600 Bangi, Selangor, Malaysia
[6]Department of Chemical Engineering, School of New Energy and Chemical Engineering, Xiamen University Malaysia, Jalan Sunsuria, Bandar Sunsuria, Sepang 43900, Selangor, Malaysia
[7]Petroleum, and Chemical Engineering, Faculty of Engineering, Universiti Teknologi Brunei, Brunei Darussalam
[8]Robert Gordon University, Garthdee House, Garthdee Road, Aberdeen, AB10 7QB, Scotland, UK

[z]E-mail: khalids@sunway.edu.my

Abstract

Recycling carbon fibre waste is crucial for sustainability in the composites industry. Herein, we report the fabrication of a heterostructure composite using recycled carbon fiber (RCF) and n-type bismuth telluride (n-Bi_2Te_3) for thermoelectric applications. In the present study, we have comprehensively investigated the effects of annealing temperature and time on the thermoelectric, structural, charge carrier transport, morphological, and thermal stability properties of annealed RCF/n-Bi_2Te_3 composites. The optimum annealing temperature and time were at 350 °C and 2 hours, respectively, which yielded a maximum power factor of 7.83 $\mu WK^{-2}m^{-1}$. Annealing redistributed the bismuth and tellurium atomic percentage, decreased carrier concentration, improved carrier mobility, enhanced the crystallinity and increased the grain size of the bismuth telluride particles, subsequently improving the thermoelectric performance as well as the thermal

stability of annealed RCF/n-Bi_2Te_3 composites. In addition, this study has explored the plausibility of a cross-plane configured Seebeck coefficient measurement utilizing recycled carbon fibre/n-type bismuth telluride heterostructure thermoelectric composite. Energy band diagram analysis indicated favorable heterojunction alignment between RCF and n-Bi_2Te_3, validating the viability of the thermoelectric composite in a cross-plane configuration. Our study provides a promising route for closing the recycling loop of carbon fiber waste and achieving sustainable thermoelectric materials.

Introduction

Carbon fiber reinforced polymer composites have emerged in various manufacturing sectors, including aerospace, automotive, wind, military, construction, and sports goods, since their discovery in the 1960s. These composites possess desirable characteristics such as high tensile strength, a favorable strength-to-weight ratio, corrosion resistance, thermal stability, and good electrical properties [1][2][3]. In anticipation of the industry's requirements, global carbon fiber production is projected to reach a volume exceeding 120,000 metric tonnes annually [4] [5], resulting in approximately 483,000 to 500,000 tonnes of carbon fibre scrap/waste generated in the next few decades [6].

However, considering the potential hazards associated with carbon fibre waste, it is not recommended to dispose of it in incineration plants due to the risk of defibrillation or oxidation, leading to the formation of tiny carcinogenic fibres. Besides, the fibres can also cause the shorting of electric flue gas filters in incinerators, posing a fire hazard. Therefore, carbon fibre wastes are normally sent for landfilling [7]. In the last decade, extensive research has also been done on recycling techniques and the performance of RCF composites. Generally, carbon fibre wastes can be recycled using mechanical, chemical (solvolysis and low-temperature chemical processing),

thermal (pyrolysis and fluidized bed) or fragmentation methods. Furthermore, the wastes can also be processed or recycled into the chopped and milled fibre, oversized tows, non-woven mats and injection moulding compounds [8,9]. Meng et al. have also reported that recovery of carbon fibre from wastes can be achieved at 5 USD/kg or less, which is around 15 % of virgin carbon fibre production cost [10]. This has shown that recycled carbon fibre (RCF) can be more economical for various applications. However, most studies have exhibited lower mechanical properties such as tensile strength, strain and fracture toughness in RCF composites than that of their virgin counterparts owing to changes in the length of the fibre, surface oxidation and char formation on fibre strands, filamentous nature of fibres which limits its reuse in critical load-bearing applications [11][12][13]. To address these limitations, incorporating polymers, nanomaterials, or hybrid materials has been explored to enhance the mechanical properties of RCF composites.

Therefore, creating a market for recycled carbon fibre composites in non-load bearing applications is imperative. Currently, recycled carbon fibre is employed in making sheet moulding compounds (SMC) [14] and in electromagnetic interference (EMI) shielding applications [15][16]. Since recycling has a minimal impact on the electrical conductivity of carbon fibres [15], and carbon fibres have also proven to exhibit a weak p-type conduction mechanism naturally [17][18], there exists a possibility of its usage also in thermoelectricity in the form of a hetero-structured thermoelectric device. Thermoelectricity is the conversion of a temperature gradient to electric voltage or vice versa. This conversion mechanism is highly desirable for energy-harvesting applications from waste heat [19].

In fact, there is a very high demand for thermoelectric materials and thermoelectric generators (TEGs) that can convert heat energy into electricity. Notably, portable and wearable devices necessitate efficient power sources, leading to the widespread utilization of TEGs. According to a

market research analysis from SNS Insider, TEGs are widely used in portable and wearable devices requiring efficient power sources. Hence, the market of TEGs is estimated to achieve 1,634 million USD by 2030 from 779 million USD in 2022, with a compound annual growth rate (CAGR) of 9.7 % [7]. The waste heat recovery segment currently dominates the TEG market, as these generators not only diminish carbon emissions but also produce valuable electricity. Achieving net zero emissions is paramount and has been legally mandated in countries such as Sweden, France, Denmark, New Zealand, and Hungary [20]. Furthermore, the automotive sector is anticipated to witness a substantial increase in demand for TEGs in the near future due to the rising popularity of hybrid and electric vehicles [7].

Bismuth telluride (Bi_2Te_3) is a well-known chalcogenide with superior thermoelectric properties at room temperature (with a figure of merit, ZT of 2.4 and 1.4 for p-type and n-type Bi_2Te_3) [21]. Although there are other reported thermoelectric materials with larger ZT, such as SnSe (4.33 at 923 K) and $Cu_{1.94}Al_{0.02}Se$ (2.62 at 1,029 K), Bi_2Te_3 has been widely used in almost all commercially available thermoelectric generators of lasers and X-ray detectors due to its high ZT value at room temperature compared to most of the other thermoelectric materials [22]. Nearly all commercially available thermoelectric generators consist of a rigid heat sink plate and rigid heat absorber plate predominantly made of ceramic with the n-type and p-type thermoelectric pellets connected via metallic interconnects and sandwiched in the middle of these plates [23]. However, ceramics as an external substrate is highly brittle and fragile and has poor flexibility and mechanical properties for prolonged usage. For other flexible polymer composite films, it requires the need of another external flexible substrate such as polyimide or Kapton will serve to attach these n and p-type flexible composite films alternatingly using metal contact (i.e., silver, etc.) paint [24][25]. The need for external substrates and in-series connection using metallic contacts in

pelletized samples and flexible composite films often complicates the fabrication process, thus making it expensive and plausibly non-scalable for practical thermoelectric conversion [26].

Therefore, in this study, we would like to capitalize on the electrically conductive nature of the RCF and n-type conduction of Bi_2Te_3 to form a hetero-structured thermoelectric device. The plausibility of recycled carbon fibre incorporation in hybrid thermoelectric composites with bismuth telluride (Bi_2Te_3) and bismuth sulphide (Bi_2S_3) have previously been investigated by the authors and have exhibited positive thermoelectric performances [27–31].

As an extension and improvement to our previously published works, we have investigated the effects on the thermoelectric performance of incorporating annealed Bi_2Te_3 thermoelectric fillers on RCF composites in this study. In the past, annealing has been known to improve the carrier transport properties [32][33], improve crystallization and structural properties [34][35], and ultimately thermoelectric performance [36][37]. However, most of the reported work in the literature has primarily focused on the effect of annealing temperature. Only very few researchers have studied the effect of varying annealing times on the thermoelectric properties of Bi_2Te_3. According to a previous compilation, the annealing temperature of Bi_2Te_3 can range from 100 ^oC to 450 ^oC, while the annealing time of those studies was mainly fixed and ranged from 2 mins to 480 minutes (8 hours) [38]. A study conducted by Sakane et al. has also applied rapid thermal annealing (RTA) of β-$FeSi_2$ doped Si nanostructure at 900 ^oC for 20 s after annealing at 600-650 ^oC for 2 mins to reduce interstitial P atoms and point defects within the structure [39]. Generally, annealing above 300 ^oC can produce the highest power factor. Therefore, the temperature ranging from 300 ^oC to 450 ^oC was chosen as the annealing temperature in this study for investigations.

This study provides a comprehensive investigation into the influence of annealing temperature and duration on various aspects of the RCF-Bi_2Te_3 composite, including its thermoelectric properties,

carrier transport properties, thermal stability, as well as structural and morphological characteristics. Notably, the thermoelectric performance of incorporating annealed semiconductor fillers into fiber-based polymer thermoelectric composites, particularly in the case of RCF, has not been reported in the existing literature. Thus, this work aims to bridge this knowledge gap and contribute to the understanding of the thermoelectric behavior of such composites.

Materials & Methods

Materials

In this study, bismuth telluride powder (Bi_2Te_3, 99.999% purity) with a relative density of 7.6 g/cm^3 and particle size of 325 mesh was obtained from Sigma Aldrich. A water-based polymeric binder, Acrodur DS 3530 (BASF, Malaysia), was used for recycled carbon fibre sheets. This study used ethylene glycol ($C_2H_6O_2$) (R&M Chemicals, Malaysia) as a solvent. Toray T600 recycled carbon fibre was sourced from Recycled Carbon Fibre Limited (RCF) Coseley, UK.

Fabrication of thermoelectric composite from recycled carbon fibre

The methodology for the fabrication was adapted from the authors' previous published works [31].

Fabrication of uncoated recycled carbon fibre composite

Several layers of recycled Toray T600 carbon fibre sheets were soaked in a mixture of water-based binder containing Acrodur DS 3530 and deionized water in a ratio of 1:10 by volume for 15 minutes. The soaked layers of recycled carbon fibre sheets were sandwiched between two metal plates covered with laboratory wipes and then subjected to a load of 10 kg to remove the excess water. This step was repeated two times to remove all residual moisture. Then, the dried layers were sandwiched between two metal plates lined with overhead projector films while subjected to

a load of 5 kg, then placed in a gravity convection oven at 200 °C for 1 hour to facilitate curing the recycled carbon fibre composite.

Annealing of Bi_2Te_3 thermoelectric fillers

The Bi_2Te_3 powder was placed in a crucible boat and then positioned in the middle of the quartz tube. The quartz tube was purged three times by nitrogen gas to remove residual contaminations within the tube, and the base pressure of the tube was maintained at 200 mTorr using a 2-stage rotary vacuum pump. Annealing was carried out in argon (purity: 99.9999%) ambient with a working pressure of 1.7 ± 2 Torr. The tubular furnace was programmed to ramp at 10 °C/min. The annealing temperature was varied at 300, 350, 400 and 450 °C for a constant annealing time of 2 hours. The temperature variation during annealing within the quartz tube was controlled at ± 1.5 °C. Thereafter, the annealing time was varied for 1, 2 and 3 hours, respectively, for the optimum annealing temperature.

Incorporation of non-annealed and annealed Bi_2Te_3 filler on recycled carbon fibre (RCF) composite

Bi_2Te_3 powder not subjected to annealing is termed non-annealed (NA) [27]. The non-annealed/annealed Bi_2Te_3 thermoelectric fillers are mixed with a binder, Acrodur DS 3530 and ethylene glycol, then sonicated in an ultrasonic water bath for 1 hour at room temperature. Then the sonicated slurry is brushed onto one side of the recycled carbon fibre composite fabricated in step 2.2.1 using the paint brushing technique. The loading of Bi_2Te_3 is 45 wt% of the composite based on the optimized study conducted previously [27]. Finally, the coated recycled carbon fibre composite is placed in the gravity convection oven at 200 °C for 1 hour to facilitate coating drying.

Measurements and Characterization

Thermoelectric Properties Measurement

Seebeck Coefficient

Seebeck coefficient was measured in a cross-plane mode with a custom-built measurement system, as shown in Figure 1. The RCF thermoelectric composite was sandwiched between two copper plates that acted as terminals. One side of the composite was heated using a Peltier module to a temperature of 40 °C (T_H), and the cold side was subjected to room temperature (T_C). The voltage difference (ΔV) resulting from this temperature difference (ΔT) is measured using a Fluke multimeter whereas the temperature difference is logged using a K-type thermocouple connected to a Picolog thermocouple data logger. The Seebeck coefficient, α is computed using the formula below, as shown in Eq (1):

$$\alpha = \frac{\Delta V}{\Delta T} = \frac{V_H - V_C}{T_H - T_C} \quad (1)$$

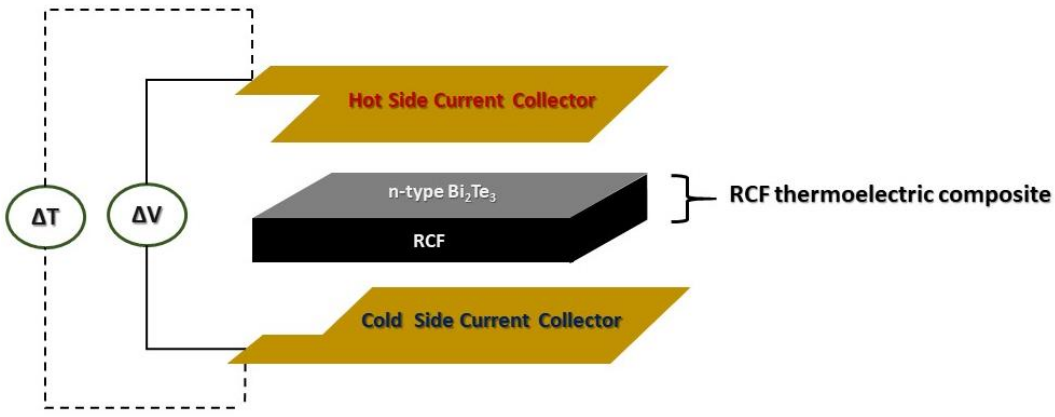

Figure 1: Schematic of the cross-section of the Seebeck coefficient measurement setup.

Electrical Resistivity and Carrier Transport Properties Measurement

The electrical resistivity (ρ) and carrier transport properties, such as carrier mobility (μ) and carrier concentration (n), were measured using the Hall effect measurement system (Ecopia, HMS 3000) at room temperature. The magnetic field strength and the probe current used are 0.57 T and 15 mA, respectively, with a delay time of 0.100 s and measurement number of 1000 times.

Power Factor

The power factor (PF) is used to gauge the performance of a thermoelectric composite and is computed using the formula below, as shown in Eq (2):

$$PF = \frac{\alpha^2}{\rho} \quad (2)$$

Material Characterizations

Field Emission Scanning Electron Microscopy (FESEM) and Energy Dispersive X-ray Spectroscopy (EDX)

The surface morphology of the RCF thermoelectric composites was studied using FESEM (FEI Quanta 400F). The elemental atomic percentage of tellurium and bismuth in the composites was studied using EDX (Oxford-Instruments INCA 400 with X-Max Detector).

X-ray Diffraction (XRD)

XRD (Cu-Kα, Bruker D8 Advance) was used to study the crystal orientation and structural properties of the RCF thermoelectric composites. The operating voltage and current were set at 40 kV and 40 mA, respectively. The XRD patterns of the RCF thermoelectric composite were studied in the range (2θ of 10° to 80°). The radiation source is Cu Kα with a step size of 0.025° and wavelength of 1.540 Å.

The crystallite size (D) was computed using Eq (3) (Scherrer equation):

$$D = \frac{0.9\lambda}{\beta cos\theta} \qquad (3) \qquad [40]$$

Where θ is the Bragg diffraction angle, β is the full width at half maximum (FWHM) of the dominant peak, and λ is the wavelength of the x-ray (1.540 Å).

The microstrain (ε) was calculated using the formula in Eq (4):

$$\varepsilon = \frac{\beta}{4\tan\theta} \qquad (4) \qquad [41]$$

Dislocation density (δ) was calculated using Eq (5):

$$\delta = \frac{1}{D^2} \qquad (5) \qquad [42]$$

Thermogravimetric Analysis (TGA)

The thermal stability properties of the thermoelectric composites were studied using a simultaneous thermal analyzer (Perkin Elmer STA 6000). The samples were tested under an air environment with a flow rate of 20 ml/min and heated from 30 °C to 900 °C with a heating ramp rate of 10 °C/min.

Results and discussions

Effect of annealing temperature on the thermoelectric properties of annealed RCF-Bi_2Te_3

The thermoelectric properties of annealed RCF-Bi_2Te_3 composites with varying annealing temperatures are shown in Figure 2 to Figure 4. As shown in Figure 2, the Seebeck coefficient increased by approximately 437% from NA to 350 °C. The increase in the Seebeck coefficient is associated with the reorganization of bismuth (Bi) and tellurium (Te) atoms during annealing. As a result, the Te atomic percent (at.%) increased from 58.42 at.% (NA) to 59.41-59.46 at.% of Te

(300 and 350 °C), as shown in Table 1. The increase in Te at.% resulted in decreased carrier concentrations from 6.01×10^{20} cm^{-3} (NA) to 1.07×10^{19} cm^{-3} (350 °C), as shown in Figure 5. The increasing Seebeck coefficient trend was also observed by [43] in Te rich Bi_2Te_3 thin films and also by [44] with increased Te particles in virgin carbon fibre based thermoelectric composite. In addition to the increase in Te content, the larger grain and or the crystallite sizes of Bi_2Te_3 particles upon annealing also led to a larger carrier mean free path that enhanced carrier mobility of electrons [34] in Bi_2Te_3 particles from 1.27×10^{-2} $cm^2V^{-1}s^{-1}$ (NA) to 9.91×10^{-1} $cm^2V^{-1}s^{-1}$ (350 °C) as shown in Figure 5, thus leading to enhanced Seebeck coefficients.

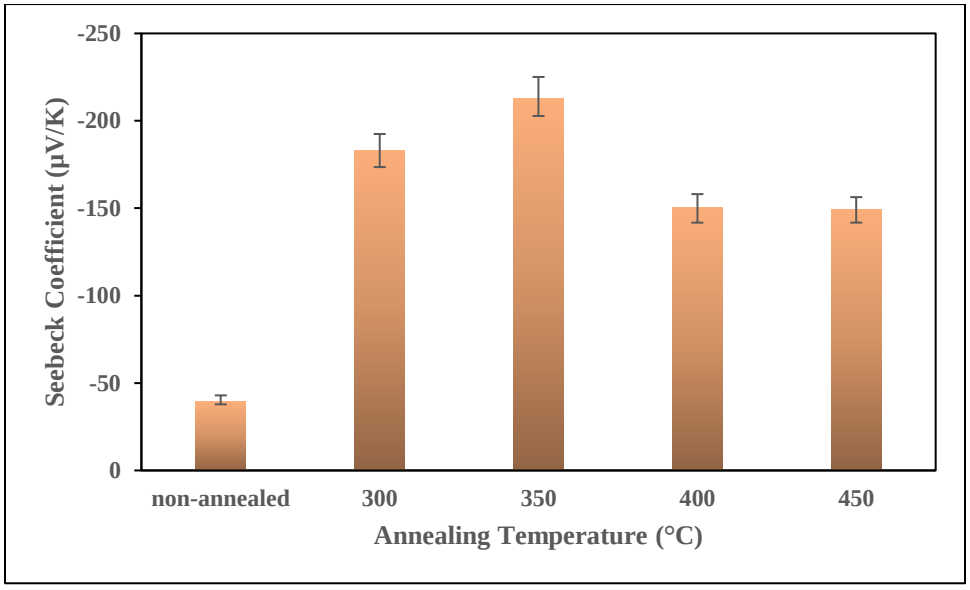

Figure 2: The influence of annealing temperature on the Seebeck coefficient of RCF-Bi_2Te_3 composites.

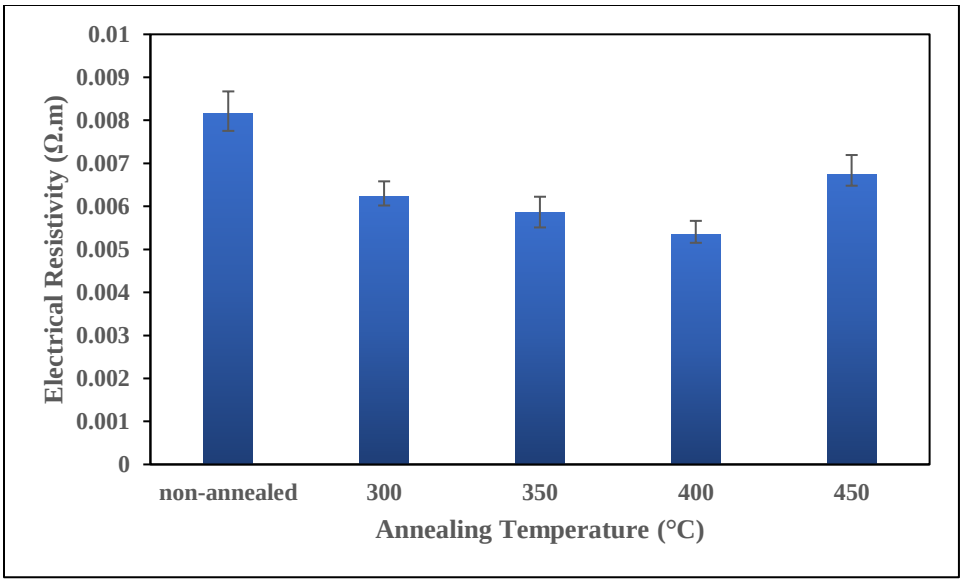

Figure 3: The influence of annealing temperature on the electrical resistivity of RCF-Bi_2Te_3 composites.

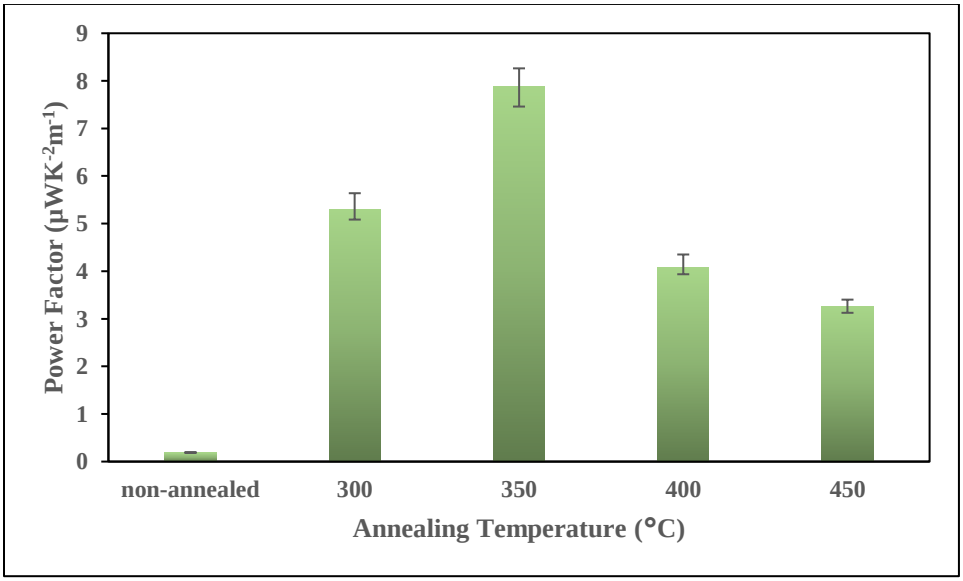

Figure 4: The influence of annealing temperature on the power factor of RCF-Bi_2Te_3 composites.

Table 1: Effect of annealing temperature on the Bi and Te content in the RCF-Bi2Te3 composites.

Annealing Temperature (°C)	Te (at %)	Bi (at %)
NA	58.42	41.58
300	59.41	40.59

350	59.46	40.54
400	58.14	41.86
450	57.61	42.39

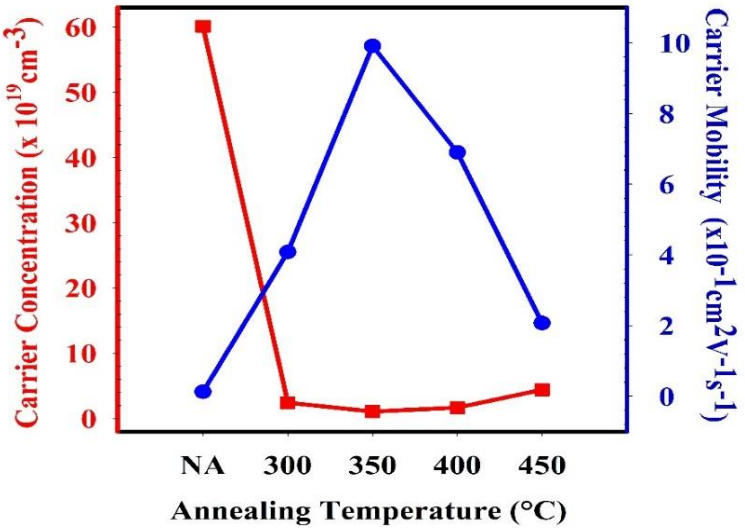

Figure 5: Carrier concentration and carrier mobility of RCF-Bi_2Te_3 composites with respect to annealing temperature.

However, at higher annealing temperatures of 400 and 450 °C, a re-evaporation of Te occurs in the annealing temperature region ranging from 400 to 450 °C [45]. This re-evaporation is proven in the EDX study (see Table 1) as the Te content decreased from 59.46 at.% (350 °C) to 57.61 at.% (450 °C). Furthermore, this decrease in Te content also resulted in an increased carrier concentration and decreased carrier mobility at 400 and 450 °C, respectively, as shown in Figure 5, thus leading to a decrease in the Seebeck coefficient beyond 350 °C as depicted in Figure 2.

The annealing process greatly improved the crystalline quality of the Bi_2Te_3 particles resulting in reduced defect vacancies and grain boundaries [46,47]. This reduction in surface defects has improved the carrier mobility within the RCF-Bi_2Te_3 composites, thus decreasing the electrical resistivity from 0.0082 Ω.m (NA) to 0.0055 Ω.m (400 °C) by approximately 33%, as shown in

Figure 3. The carrier mobility improved by one order from 1.27×10^{-2} $cm^2V^{-1}s^{-1}$ (NA) to 9.91×10^{-1} $cm^2V^{-1}s^{-1}$ (350 °C), as shown in Figure 5. A similar decrease in electrical resistivity upon annealing is observed in Bi_2Te_3 films obtained by electrodeposition [38] and RF magnetron sputtering [39] due to the annealing-induced reduction in defect vacancies. However, at 450 °C, the electrical resistivity of RCF-Bi_2Te_3 composites increased as compared to 400 °C perhaps owing to surface defects that were induced due to lack of stoichiometry at higher annealing temperatures thus reducing the carrier mobility,

The power factor of RCF-Bi_2Te_3 composites was greatly enhanced from 0.194 $\mu WK^{-2}m^{-1}$ (NA) to 7.821 $\mu WK^{-2}m^{-1}$ (350 °C) by approximately 3930%, as shown in Figure 4. This increment in power factor is due to the improvement in grain growth that occurs during annealing, thus altering its electron transport behaviour [48]. Beyond 350 °C, the power factors are seen to decrease at higher annealing temperatures of 400 and 450 °C. At elevated annealing temperatures, the atomic proportion of Te experienced a decremental trend, as evidenced by the data presented in Table 1, which can be attributed to the process of Te evaporation. This occurs because the evaporation energy of Te (1)(52.55 kJ/mol) is approximately two times lower than that of Bi (104.80 kJ/mol) in the rhombohedral layered structure of -Te(1)-Bi-Te(2)-Bi-Te(1)-, thus making it easier for Te to evaporate [45,49]. Therefore, the imbalance in the stoichiometry of Bi_2Te_3 at higher temperatures has decreased power factors at 400 and 450 °C. The optimum annealing temperature for RCF-Bi_2Te_3 composites is 350 °C.

Effect of annealing temperature on the morphology of annealed RCF-Bi_2Te_3 composites

Figure 6 below shows the surface morphology images of RCF-Bi_2Te_3 composites annealed at different temperatures.

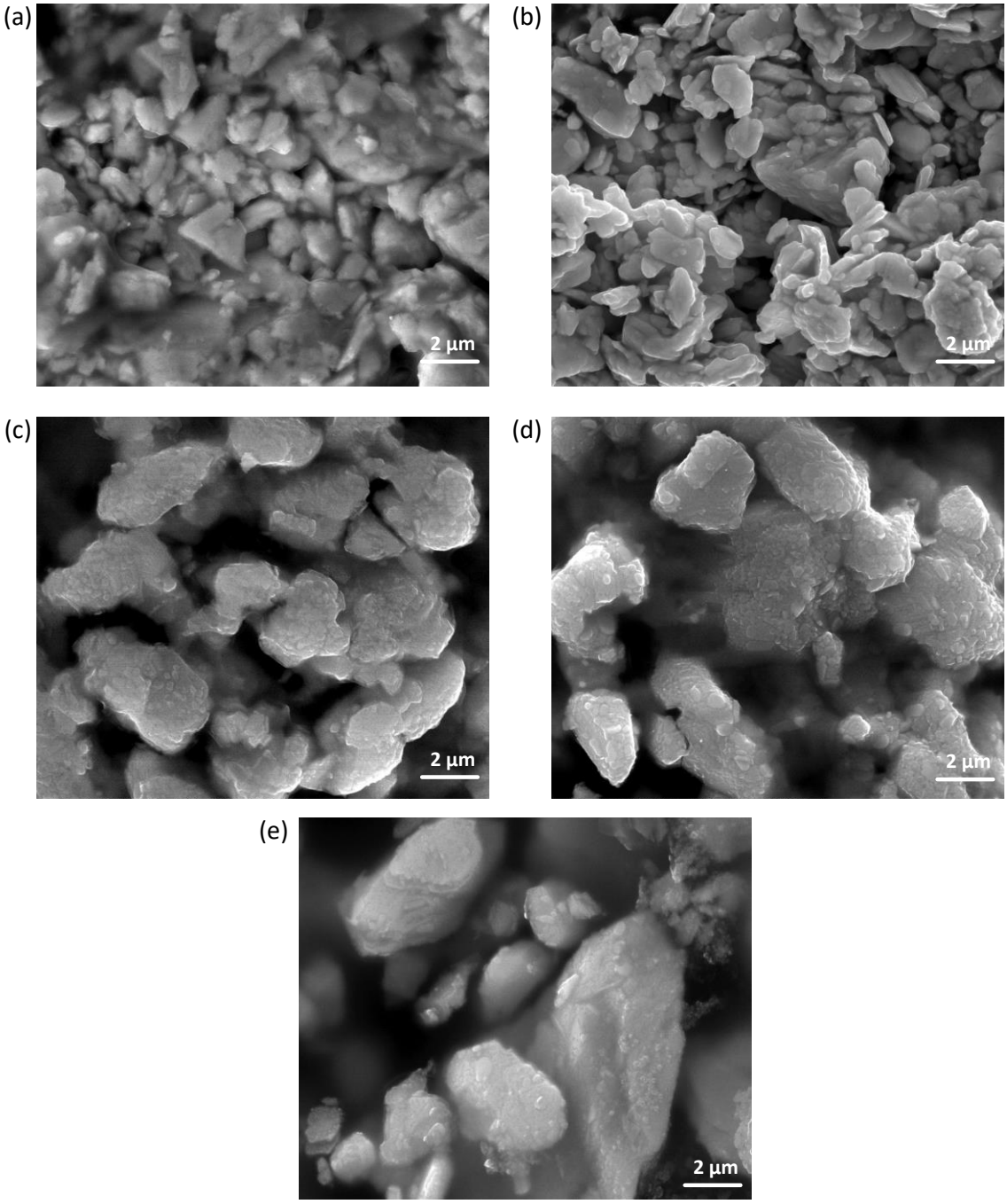

Figure 6: FESEM surface images of RCF-Bi_2Te_3 composites non-annealed (a) NA and annealed at (b) 300 °C (c) 350 °C (d) 400 °C (e) 450 °C.

The augmentation of thermal energy during annealing has facilitated the amalgamation of submicron grains, thereby forming larger grains, as depicted in Figure 6 (b). This contrasts with the individualized submicron grains evident in the NA sample illustrated in Figure 6 (a). These

findings are in agreement with previous studies [43]. The grain size of Bi_2Te_3 particles increased with respect to the increase in annealing temperature, as shown in Figures 6 (b) to (e). There were also fewer grain boundaries observed in the FESEM images with the increment in grain size, leading to improved carrier mobility that ultimately led to a decrement in the electrical resistivity upon annealing, as shown in Figure 3. A similar agglomeration of grains and grain size improvement was observed by Wang et al. [39] with annealed sputtered Bi_2Te_3 films and Rashid et al. [46] with electrodeposited Bi_2Te_3 films that were rapid thermally annealed.

Effect of annealing temperature on the XRD analysis of annealed RCF-Bi_2Te_3 composites

X-ray diffraction (XRD) patterns of RCF-Bi_2Te_3 (NA) and annealed RCF-Bi_2Te_3 with respect to different annealing temperatures at a constant annealing time of 2 hours are shown in Figure 7. Figure 7 depicts 12 distinct diffraction peaks located at 2θ of 17.59°, 27.78°, 37.93°, 40.42°, 41.27°, 44.64°, 50.37°, 54.00°, 57.17°, 62.31°, 66.04° and 67.17° with orientations of (006), (015), (1010), (0111), (110), (0015), (205), (1016), (0210), (1115), (0120) and (125). The obtained diffraction peaks are compared to the standard data of the Joint Committee on Powder Diffraction Standards (PDF 00-015-0863), confirming the presence of Bi_2Te_3 [50]. All the XRD related parameters below are calculated with respect to the dominant peak (015) obtained in this study.

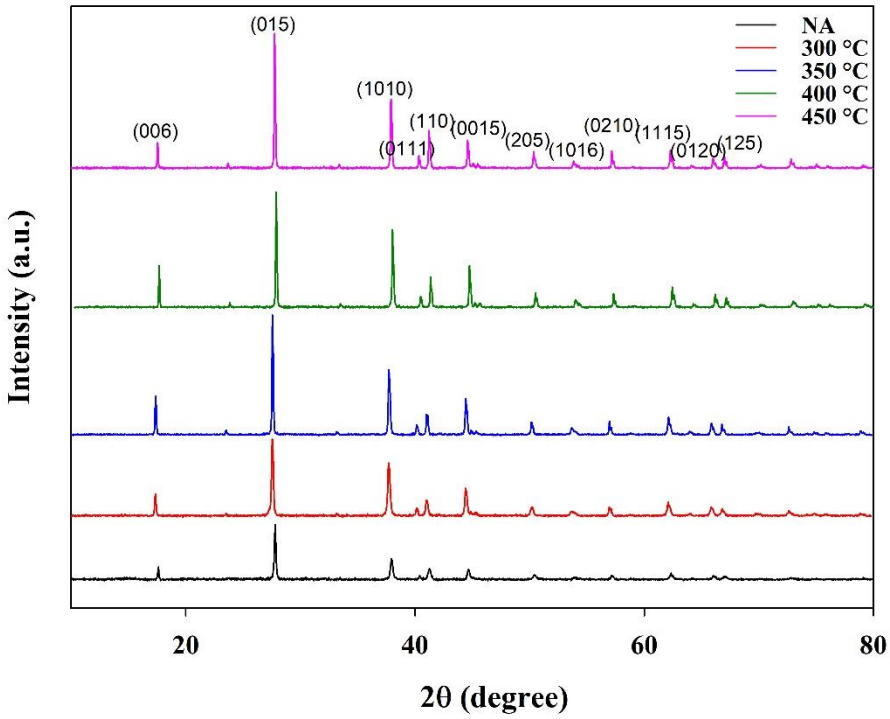

Figure 7: XRD patterns of RCF-Bi_2Te_3 composites with respect to different annealing temperatures.

The D, ε and δ of the non-annealed and annealed RCF-Bi_2Te_3 composites with respect to different annealing temperatures are shown in Table 2.

Table 2: Structural properties of RCF-Bi_2Te_3 with respect to varying annealing temperatures.

Annealing Temperature (°C)	FWHM (radian)	Crystallite size, D (nm)	Microstrain (ε x 10^{-3}) ($lines^{-2}\ m^{-4}$)	Dislocation density (δ x 10^{14}) ($lines/m^2$)
NA	0.0030	47.01	3.1	4.52
300	0.0026	54.88	2.6	3.32
350	0.0023	61.94	2.3	2.61
400	0.0024	60.13	2.4	2.78
450	0.0023	62.89	2.3	2.53

The crystallization of Bi_2Te_3 particles in the RCF-Bi_2Te_3 composites improved upon annealing, which is proven by the increase in the intensity of XRD peaks for all annealed samples, as shown in Figure 7. Upon annealing, the increase in temperature accelerated the diffusion and

agglomeration of the Bi_2Te_3 atoms, leading to the above mentioned increase in crystallinity. As a result, all of the samples exhibited a polycrystalline nature. This increase in crystallinity upon annealing is also further validated with a decrement in the FWHM values upon annealing, as shown in Table 2. The FWHM decreased from 0.0030 rad (NA) to 0.0023 rad (350 °C). A similar increase in the intensity of XRD peaks due to improved crystallinity owing to annealing was also observed [51–53].

Figure 7 also shows a slight shift in the XRD peaks, which is in line with the change in Bi and Te content as depicted in Table 1 upon annealing. For example, the 2θ angle for 015 plane in stoichiometric Bi_2Te_3 (PDF 00-015-0863) with 60 at.% of Te and 40 at.% of Bi is 27.564°. The 015 plane at annealing temperatures of 300 and 350 °C has 2θ at 27.545° that is closest to stoichiometric 2θ at 27.564°. Thus, it is observed in Figure 7 the XRD peaks shift from right (NA) to left (300 and 350 °C) upon annealing. Beyond 350 °C, the XRD peaks shift again towards the right side due to the volatility of Te and subsequent off-stoichiometry content of Bi and Te. The phenomenon of XRD peak shifting as a result of annealing was also observed by Rashid et al. The change of the peak positions are due to the crystalline change in the composite after the annealing treatment [46].

As shown in Table 2, the crystallite size also increased upon annealing from 47.01 nm (NA) to 62.89 nm (450 °C). When annealed, the increase in D results from the agglomeration and enlargement of Bi_2Te_3 grains. During the annealing process, the crystal size increase and grain boundary reduction also result in a larger effective mean free path for carriers, thus improving its carrier mobility [34,51,54]. The improved carrier mobility resulted in an increased Seebeck coefficient and reduced electrical resistivity simultaneously, as shown in Figure 2 and Figure 3, respectively.

The microstrain, ε and dislocation density, δ, as shown in Table 2, were also seen to decrease with respect to the increase in annealing temperature. Both ε and δ decreased tremendously from NA to 350 °C, owing to the reduction in lattice imperfection and defects commonly attributed to annealing [54]. The decrease in ε and δ also resulted in a subsequent decrease in the electrical resistivity of the annealed RCF-Bi_2Te_3 composites until 400 °C as shown in Figure 3.

Effect of annealing temperature on the thermal stability of annealed RCF-Bi_2Te_3 composites

The thermal stabilities of annealed RCF-Bi_2Te_3 composites were evaluated using thermogravimetric analysis (TGA) and derivative thermogravimetric (DTG) studies. The TGA results for annealed and non-annealed (NA) RCF-Bi_2Te_3 composites with respect to annealing temperatures are shown in Figure 8.

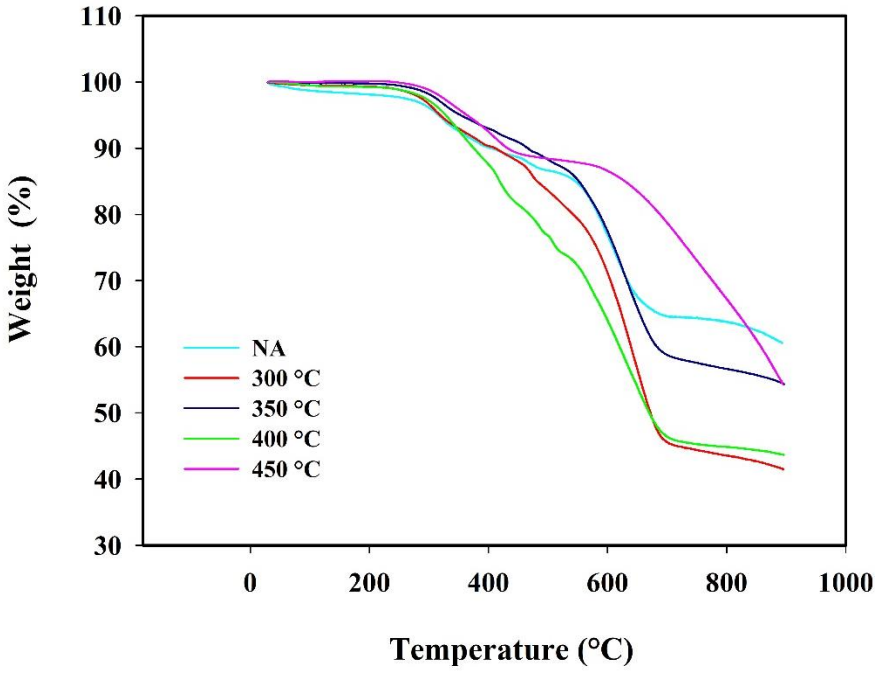

Figure 8: TGA curves of RCF-Bi_2Te_3 composites annealed at different temperatures.

Based on Figure 8, annealing improved the onset degradation temperature (T_{onset}), T_{onset} is the initial temperature at which the composite exhibits a characteristic mass loss of 5% [27]. The T_{onset}

improved from 316.2 °C (NA) to 363.83 °C (450 °C). The improvement in T_{onset} may be probable because of the evaporation of volatile and weakly bonded Bi and Te atoms after annealing, especially for RCF-Bi_2Te_3 composites annealed at higher temperatures. For example, for RCF-Bi_2Te_3 composite annealed at 450 °C, there is a peculiar increase in the T_{onset} plausibly because most volatile bonds may have evaporated at 400 °C, resulting in the formation of a more thermally stable compound at 450 °C. However, this thermally improved structure has adverse thermoelectric properties, as shown in Figures 2 to 4.

The improvement in thermal stability of annealed RCF-Bi_2Te_3 composite is also highlighted in the improvement of the maximum degradation temperature (T_{max}) of the composites upon annealing, as shown in Figure 9. T_{max} is the temperature at which the composite experiences a maximum weight loss, denoted by the peak of derivative (dW/dT) curve [27]. All annealed DTG curves shifted to the right compared to the NA curve, denoting an improvement in T_{max}. The T_{max} increased from 602.19 °C (NA) to approximately 630 °C (300, 350 and 400 °C). However, at 450 °C, there is an extreme shift to the right at which the T_{max} was unable to be obtained due to the limitation of the TGA equipment with a maximum measurement temperature range of up to 1000 °C. Hence, it can be hypothesized that at 450 °C, a much more thermally stable compound is produced with a marginally larger T_{max} than the rest of the annealed samples. However, though thermally more stable, the Bi_2Te_3 structure annealed at 450 °C may have lost elements and bonds responsible for thermoelectric capabilities, as proven by its poor thermoelectric performance at this annealing temperature.

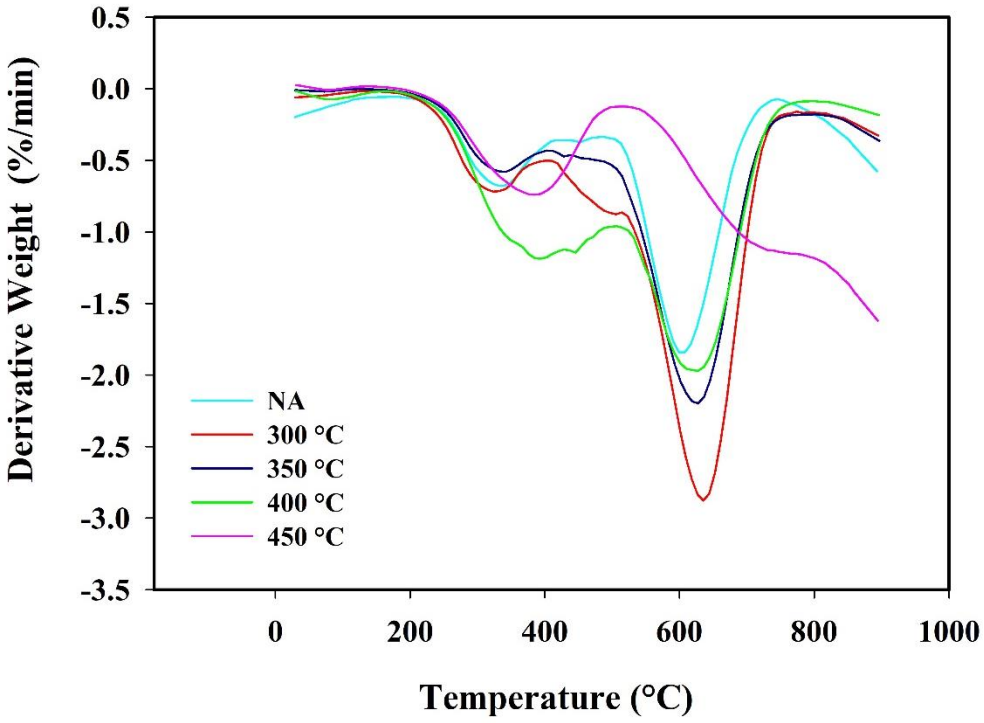

Figure 9: DTG curves of RCF-Bi_2Te_3 composites annealed at various temperatures.

Effect of annealing time on the thermoelectric properties of annealed RCF-Bi_2Te_3

As observed in , the optimum annealing temperature for RCF-Bi_2Te_3 composites is 350 °C. Thus, this section studied the effect of varying annealing times (1, 2 and 3 hours) at an annealing temperature of 350 °C. The influence of annealing time on the Seebeck coefficient is illustrated in Figure 10. The results show that all annealed samples are n-type with a negative Seebeck coefficient. As the annealing time increased, the Seebeck coefficient increased from -39.84 µV/K (NA) to a maximum of -214.27 µV/K (2 hours), denoting a 437% improvement in the Seebeck coefficient.

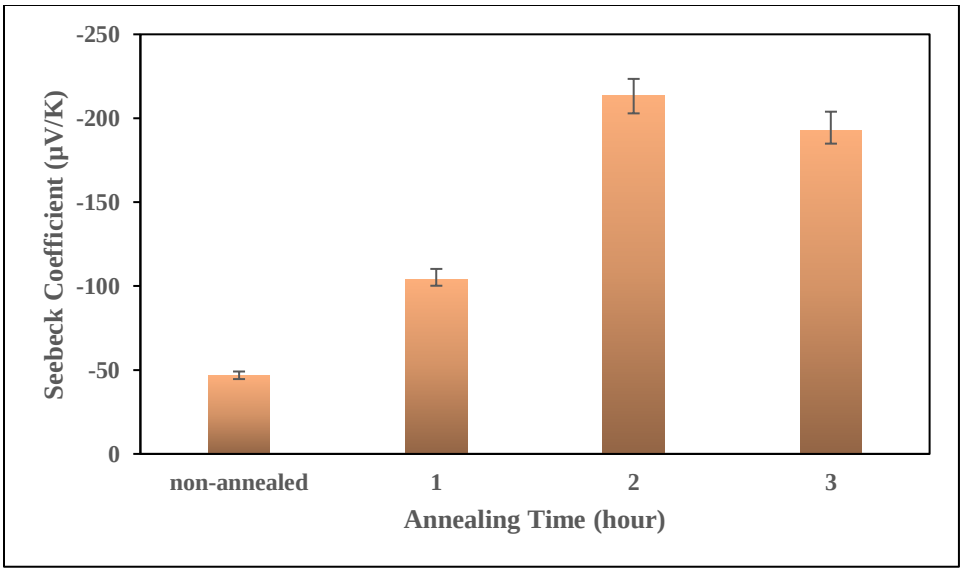

Figure 10: The influence of annealing time on the Seebeck coefficient of RCF-Bi_2Te_3 composites.

Heat energy supplied during annealing allowed for the redistribution and reorganization of bismuth and tellurium atoms. As a result, the tellurium content increased from 58.42 at.% (NA) to 59.46 at.% (2 hours), as shown in Table 3. The increase in tellurium content also led to a subsequent decrease in the carrier concentration from 6.01×10^{20} cm^{-3} (NA) to 1.15×10^{19} cm^{-3} (2 hours), as depicted in Figure 11, resulting in the increased Seebeck coefficient. A similar decrease in carrier concentration after annealing was also observed for sputtered n-type Bi_2Te_3 thin films [37] and also for Bi_2Te_3 nanoplate films synthesized from a combination of solvothermal and electrodeposition [55].

Table 3: Effect of annealing time on the Bi and Te content in the RCF-Bi_2Te_3 composites.

Annealing Time (hour)	Te (at %)	Bi (at %)
NA	58.42	41.58
1	59.1	40.9
2	59.46	40.54
3	58.88	41.12

The prolonged exposure to heat at 350 °C led to slight evaporation of Te from 59.46 at.% (2 hours) to 58.88 at.% (3 hours), as shown in Table 3. Though Te element tends to sublime out of Bi_2Te_3 at temperatures higher than 400 °C due to its low melting point and high evaporation pressure, as previously reported by [56,57], however Ohsugi et al. [58] have reported the plausibility of Te sublimation at temperatures lower than 400 °C. This is because, within the Bi_2Te_3 structure, the thermal expansion perpendicular to the Te layers is more prominent than the thermal expansion parallel to the tellurium layers. Thus spacing between tellurium layers is increased when subjected to heating, leading to the loss of Te at a faster rate than that of Bi. In addition to the thermal expansion, Te easily sublimes out due to the weak van der Waals bond between neighbouring tellurium layers in the Bi_2Te_3 structure [49,51]. The evaporation Te is also accompanied by the increase in carrier concentration from 1.15×10^{19} cm^{-3} (2 hours) to 1.35×10^{19} cm^{-3} (3 hours), as shown in Figure 11. Each tellurium vacancy (V_{Te}) generates two electrons per defect [49], thus contributing to the overall increase in carrier concentration and subsequent decrease in the Seebeck coefficient at 3 hours, as depicted in Figure 10.

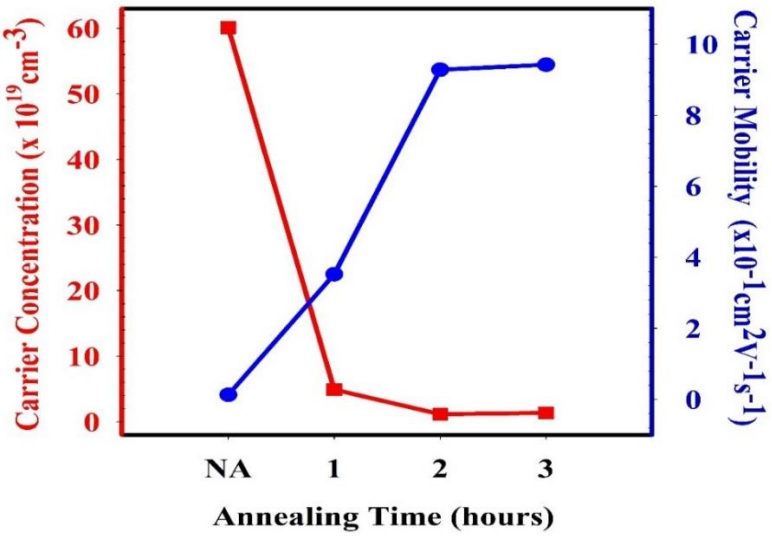

Figure 11: Carrier concentration and carrier mobility of RCF-Bi_2Te_3 composites with respect to annealing time.

The influence of annealing time on the electrical resistivity is illustrated in Figure 12. The electrical resistivity initially was reduced by approximately 56% from 0.0082 Ω.m (NA) to 0.0036 Ω.m (1 hour). This decrease in resistivity is attributed to the 2671% enhancement in carrier mobility from 1.27×10^{-2} $cm^2V^{-1}s^{-1}$ (NA) to 3.52×10^{-1} $cm^2V^{-1}s^{-1}$ (1 hour), though annealing decreased the carrier concentration of Bi_2Te_3 particles, however as the improvement in carrier mobility was larger than the percentage drop in carrier concentration thus decreasing the overall electrical resistivity of the RCF-Bi_2Te_3 composite. A similar improvement in electrical resistivity with decreased carrier concentration and improved carrier mobility was also observed in annealed Bi_2Te_3 nanoplate films grown using molecular beam epitaxy owing to the crystallization that takes place during annealing [32].

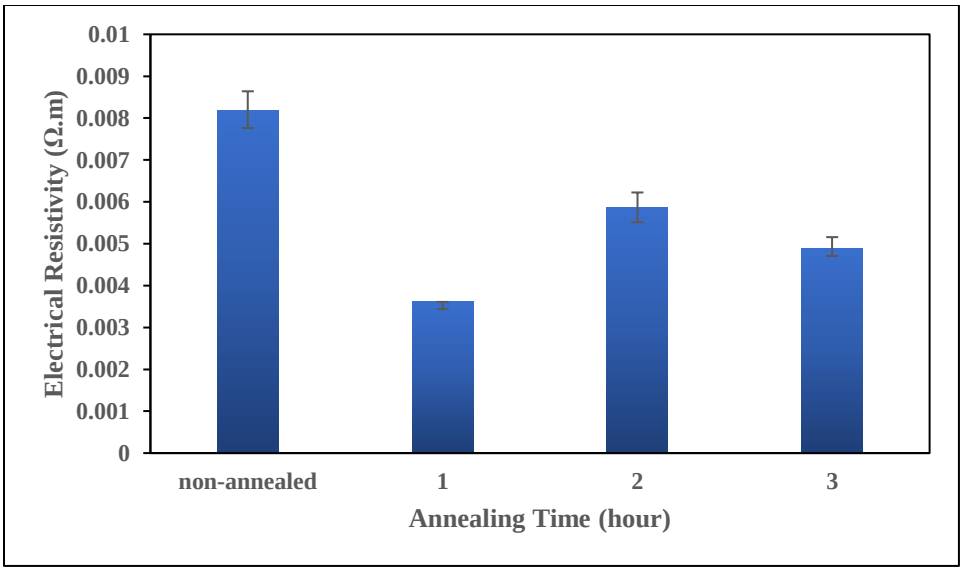

Figure 12: The influence of annealing time on the electrical resistivity of RCF-Bi_2Te_3 composites.

In addition to the carrier transport properties, annealing also improved the bismuth and tellurium content to more stoichiometric proportions from 58.42 at.% of Te (NA) to 59.1 at.% of Te (1 hour), as shown in Table 3, resulting in lower carrier trapping and a defect free band gap allowing electrons to transfer efficiently from the valence band to the conduction band. A marginal rise in resistivity from 0.0036 Ω.m (1 hour) to 0.0059 Ω.m (2 hours) was observed after annealing for 2 hours. This can be attributed to the decrease in carrier concentration from the annealing process. Prolonged annealing at 350 °C beyond 2 hours resulted in tellurium evaporation, and the tellurium decreased from 59.46 at.% (2 hours) to 58.88 at.% (3 hours) shown in Table 3. However, as the bismuth content increases in the bismuth telluride alloy owing to the evaporation of Te, it depicts a metallic property with a corresponding increase in carrier concentration from 1.15×10^{19} cm^{-3} (2 hours) to 1.35×10^{19} cm^{-3} (3 hours) resulting in reduced electrical resistivity as shown in Figure 12.

The influence of annealing time on the power factor is illustrated in Figure 13. The power factor increases with respect to annealing duration and reaches a maximum power factor of 7.80 $\mu WK^{-2}m^{-1}$ and 7.83 $\mu WK^{-2}m^{-1}$ for 2 and 3 hours, respectively. All annealed samples exhibited a higher power factor than the non-annealed counterpart owing to annealing-induced nucleation, grain growth and redistribution of bismuth and tellurium atoms. However, annealing beyond two hours leads to tellurium loss, alters the stoichiometry of Bi_2Te_3 and slightly decreases the power factor, which is not favourable for its thermoelectric properties. Thus the optimum annealing time for RCF-Bi_2Te_3 composites is 2 hours.

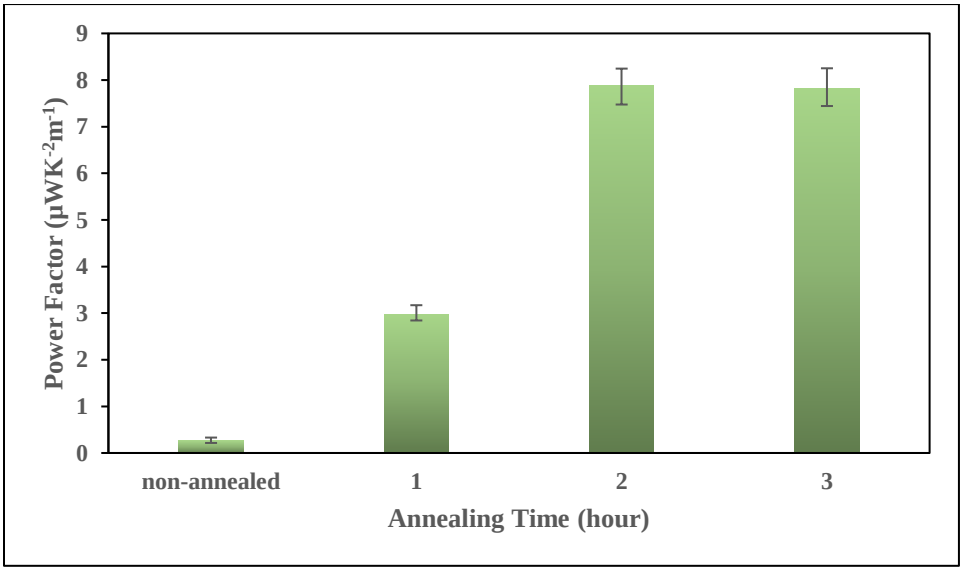

Figure 13: The influence of annealing time on the power factor of RCF-Bi_2Te_3 composites.

Effect of annealing time on the morphology of annealed RCF-Bi_2Te_3 composites

Figure 14 shows the surface morphology images of RCF-Bi_2Te_3 composites annealed at 350 °C with varying annealing duration.

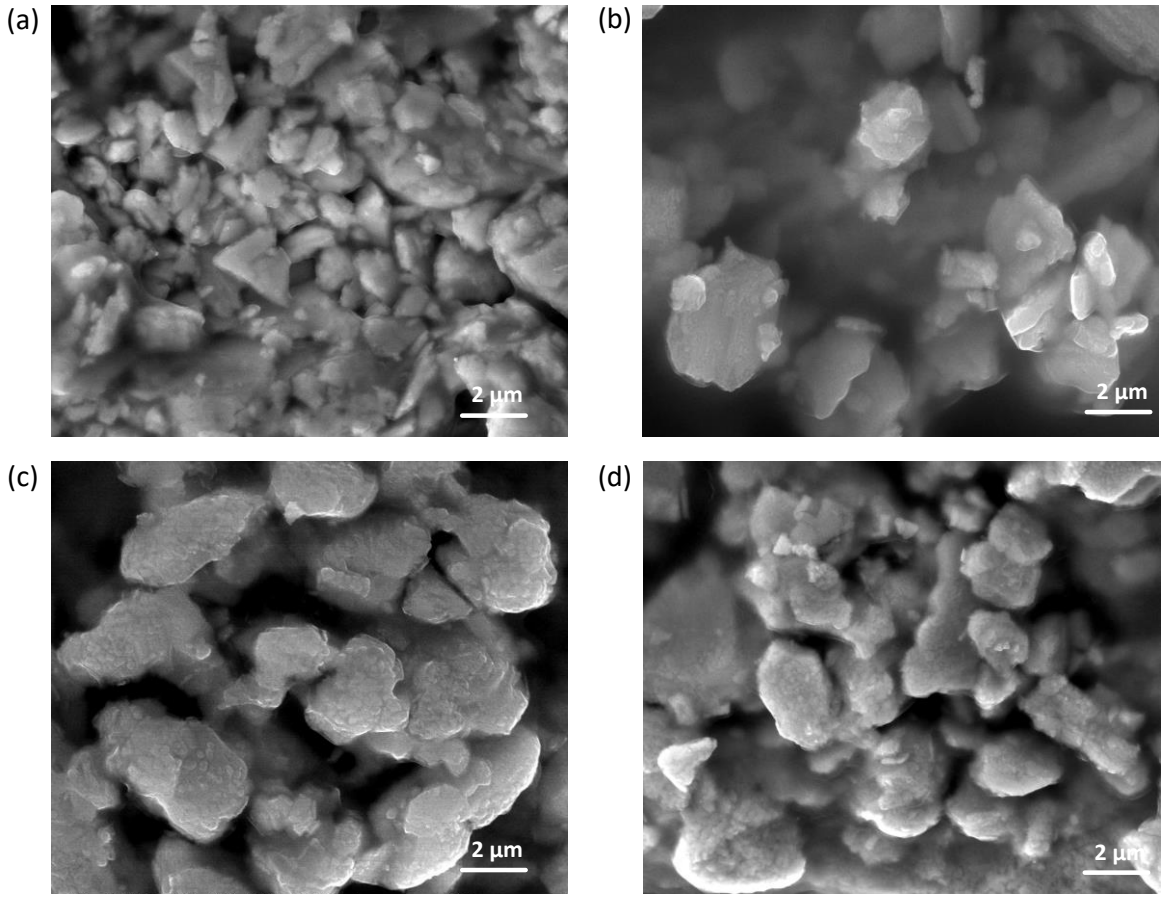

Figure 14: FESEM surface images of RCF-Bi_2Te_3 composites non-annealed (a) NA and annealed at 350 °C for (b) 1 hour (c) 2 hours (d) 3 hours.

The present study investigates the influence of annealing on the grain size of Bi_2Te_3 particles. Our results demonstrate that all annealed Bi_2Te_3 particles exhibit a larger grain size compared to their non-annealed counterparts. Moreover, the observed grain size positively correlates with annealing duration, as illustrated in Figure 14. A similar improvement in grain size after annealing was also observed in the surface morphology studies for Bi_2Te_3 thin films synthesized via thermal evaporation [34] and electrochemical deposition [59] owing to nucleation of grains with the increase in thermal energy. The increment in grain size upon annealing led to decreased density of grain boundaries, thus resulting in a one-order improvement in carrier mobility for all annealed

samples from 1.27×10^{-2} $cm^2V^{-1}s^{-1}$ (NA) to a maximum of 9.42×10^{-1} $cm^2V^{-1}s^{-1}$ (3 hours) as shown in Figure 11. When there are fewer grain boundaries, there are fewer scattering centres, thus requiring lower energy when electrons move from one grain to the other resulting in improved carrier mobility. The improved carrier mobility resulted in a simultaneous increase in both Seebeck coefficient and decreased electrical resistivity, as shown in Figure 10 and Figure 12, resulting in higher power factors for annealed RCF-Bi_2Te_3 composites, as shown in Figure 13. The optimum annealing duration is 2 hours as there was no significant improvement in grain growth between 2 and 3 hours, which was also reflected in its power factor that remained almost constant with a slight decrease at 3 hours, as shown in Figure 13.

Effect of annealing time on the XRD analysis of annealed RCF-Bi_2Te_3 composites

X-ray diffraction (XRD) patterns of RCF-Bi_2Te_3 non-annealed (NA) and annealed RCF-Bi_2Te_3 with respect to different annealing durations at a constant annealing temperature of 350 °C is as shown in Figure 15. It depicts 12 distinct diffraction peaks located at 2θ of 17.59°, 27.78°, 37.93°, 40.42°, 41.27°, 44.64°, 50.37°, 54.00°, 57.17°, 62.31°, 66.04° and 67.17° with orientations of (006), (015), (1010), (0111), (110), (0015), (205), (1016), (0210), (1115), (0120) and (125). The obtained diffraction peaks are compared to the standard data of the Joint Committee on Powder Diffraction Standards (PDF 00-015-0863), confirming the presence of Bi_2Te_3 [50]. All the XRD related parameters below are calculated with respect to the dominant peak (015) obtained in this study.

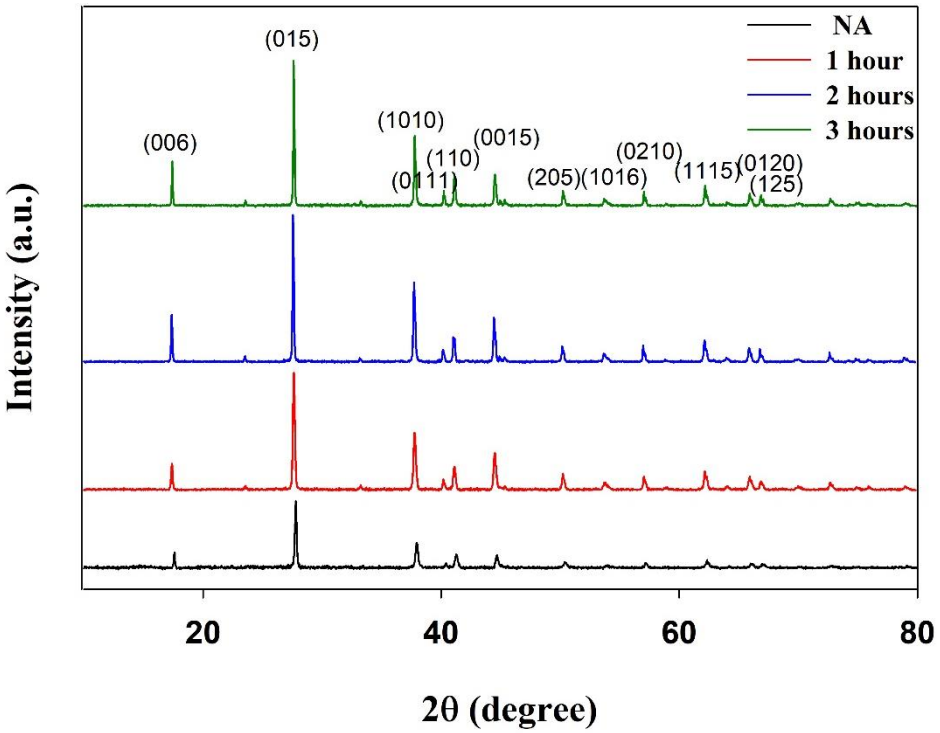

Figure 15: XRD patterns of RCF-Bi_2Te_3 composite annealed at 350 °C for varying annealing durations.

The D, ε and δ of the NA RCF-Bi_2Te_3 and annealed RCF-Bi_2Te_3 composites with respect to different annealing durations are shown in Table 4.

Table 4: Structural properties of the NA RCF-Bi_2Te_3 and annealed RCF-Bi_2Te_3 at 350 °C with varying annealing durations.

Annealing Time (hours)	FWHM (radian)	Crystallite size, D (nm)	Microstrain (ε x 10^{-3}) ($lines^{-2}\ m^{-4}$)	Dislocation density (δ x 10^{14}) ($lines/m^2$)
NA	0.0030	47.01	3.1	4.52
1	0.0029	49.56	2.9	4.07
2	0.0023	61.94	2.3	2.60
3	0.0022	63.89	2.3	2.45

All annealed samples exhibited higher peak intensities than the non-annealed sample, as shown in Figure 15. The crystallinity of samples also increased with increasing annealing duration, which

resulted in decreased FWHM values from 0.0030 (NA) to 0.0022 (3 hours), as shown in Table 4. The improvement in crystallinity is due to the high thermal energy supplied during annealing that enhanced crystallization of the Bi_2Te_3 particles, leading to sharp and narrower peaks in the XRD pattern and corresponding lower FWHM values. There was no improvement in crystallinity in samples annealed at 2 and 3 hours, as the FWHM remained at 0.0022-0.0023, as shown in Table 4.

Table 4 demonstrates that all annealed samples' crystallite size, D, was greater than that of the non-annealed sample. The size of D increased from 47.01 nm (NA) to 63.89 nm (3 hours). This increase in D is attributed to the agglomeration and enlargement of Bi_2Te_3 grains during annealing. This is also reflected in the larger grain size of annealed Bi_2Te_3 particles, as shown in Figure 14. With larger grain sizes, there is a reduction in grain boundaries and larger effective mean free path for carrier transportation, which is reflected in the improvement in carrier mobility from 1.27×10^{-2} $cm^2V^{-1}s^{-1}$ (NA) to 9.42×10^{-1} $cm^2V^{-1}s^{-1}$ (3 hours) as shown in Figure 11.

The microstrain, ε and dislocation density, δ, as shown in Table 4, declined with respect to the increase in annealing duration. The decrease in ε and δ is due to the reduction in lattice defects upon annealing. Amorphous-like materials are known to contain large defects with higher carrier concentrations [60]. However, with annealing, as the crystallinity is improved and the amorphous phase is reduced, there will be lower defects within the lattice structure of Bi_2Te_3. However, decreasing ε and δ did not reduce the electrical resistivity of annealed RCF-Bi_2Te_3 composites with respect to annealing duration beyond 1 hour, as shown in Figure 12. Instead, the electrical resistivity increased due to the massive decrease in carrier concentration. Despite the increase in electrical resistivity, all annealed RCF-Bi_2Te_3 composites exhibited a higher power factor than the

non-annealed sample, as shown in Figure 13, due to reduced lattice defects that improved carrier mobility by one order compared to its non-annealed counterpart.

Effect of annealing time on the thermal stability of annealed RCF-Bi_2Te_3 composites

The thermal stabilities of RCF-Bi_2Te_3 composites annealed at 350 °C with varying durations were evaluated using thermogravimetric analysis (TGA) and derivative thermogravimetric (DTG) studies. The TGA results for annealed and non-annealed (NA) RCF-Bi_2Te_3 composites with respect to annealing time are shown in Figure 16.

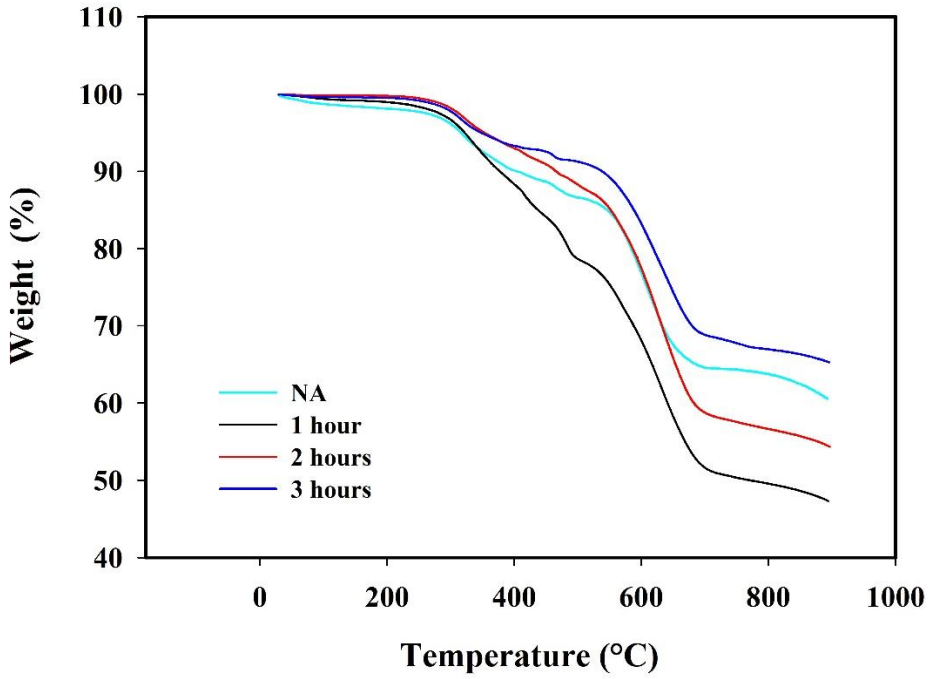

Figure 16: TGA curves of RCF-Bi_2Te_3 composites annealed at different durations.

Based on Figure 16, annealing improved the onset degradation temperature (T_{onset}) at 5% mass loss in RCF-Bi_2Te_3 composites from 316.2 °C (NA) to 353.16 °C (2 hours). The improvement in T_{onset} could be attributed to the evaporation of volatile and weakly bonded elements during

annealing (heat treatment). However, after two hours, the T_{onset} slightly decreased from 353.16 °C (2 hours) to 347.94 °C (3 hours).

The improvement in thermal stability of annealed RCF-Bi_2Te_3 composite is also highlighted in the improvement of the maximum degradation temperature (T_{max}) of the composites as shown in Figure 17. All annealed DTG curves shifted to the right compared to the non-annealed curve, denoting an improvement in T_{max}. The T_{max} increased from 602.19 °C (NA) to approximately 630 °C (1,2 and 3 hours). There was no observable change in T_{max} with varying annealing duration. Both TGA and DTG results indicate that removing volatile elements within the Bi_2Te_3 structure during annealing improved the thermal stability of the thermoelectric composites.

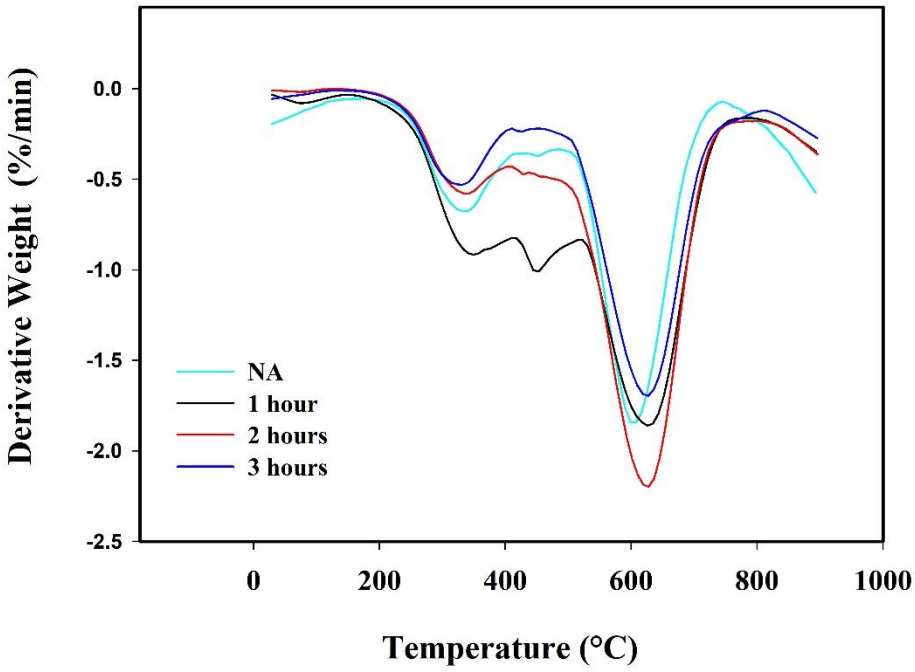

Figure 17: DTG curves of RCF-Bi_2Te_3 composites annealed at various durations.

RCF/n-Bi_2Te_3 heterojunction band structure

A majority of reported studies in the literature thus far have only reported an in-plane configuration for the measurement of the Seebeck coefficient as it is predominantly focused on a singular semi-conducting behaviour, either n-type or p-type in the form of thin films, pellets or flexible films [37][61][62]. However, this study primarily adopted a cross-plane measurement configuration to validate the feasibility of RCF/n-Bi_2Te_3 heterostructure as a thermoelectric device. A similar cross-plane measurement configuration for the Seebeck coefficient was previously reported only for virgin carbon fibre and also glass fibre based thermoelectric composites [44][63] [18]. However, these studies did not report the band and electronic structure of its thermoelectric composites. As presented in our result and discussion, RCF/n-Bi_2Te_3 heterostructure thermoelectric composite has recorded an optimal power factor of 7.836 $\mu WK^{-2}m^{-1}$, indicative of a favourable heterojunction formation for thermally induced charge carrier transport. Herewith, we attempt to elucidate the possible heterojunction energy band diagram of RCF/n-Bi_2Te_3 heterostructure thermoelectric composite, as shown in Figure 18. Figure 18 (a) depicts the electronic property of RCF and n-Bi_2Te_3 prior to junction formation. Work functions, Φ of RCF and n-Bi_2Te_3 were obtained from literature to be 4.95 eV, and 5.12 eV, respectively [64][65], whereas the optical band gap of n-Bi_2Te_3 is 0.17 eV [65]. Due to the n-type conductivity of Bi_2Te_3 in this study, the Fermi level, E_F is located in the vicinity of the conduction band edge, E_C. One of the prerequisites for energy band alignment in thermal equilibrium is the formation of a flat E_F ($dE_F/dx = 0$) across the heterostructure [66]. Hence, to accommodate the aforesaid condition, a downward band bending of E_C and valence band edge, E_V, in the vicinity of RCF/n-Bi_2Te_3 hetero-interface occurs, as shown in Figure 18 (b). Figure 18 (c) illustrates the energy band diagram of RCF/n-Bi_2Te_3 heterostructure thermoelectric composite when subjected to a thermal gradient in an open circuit condition akin

to the Seebeck coefficient measurement setup. When n-Bi_2Te_3 is subjected to a higher temperature, thermal excitation of electrons from the E_V to E_C occurs and subsequently results in increased minority (holes in valence band (VB)) and majority (electrons in conduction band (CB)) carriers.

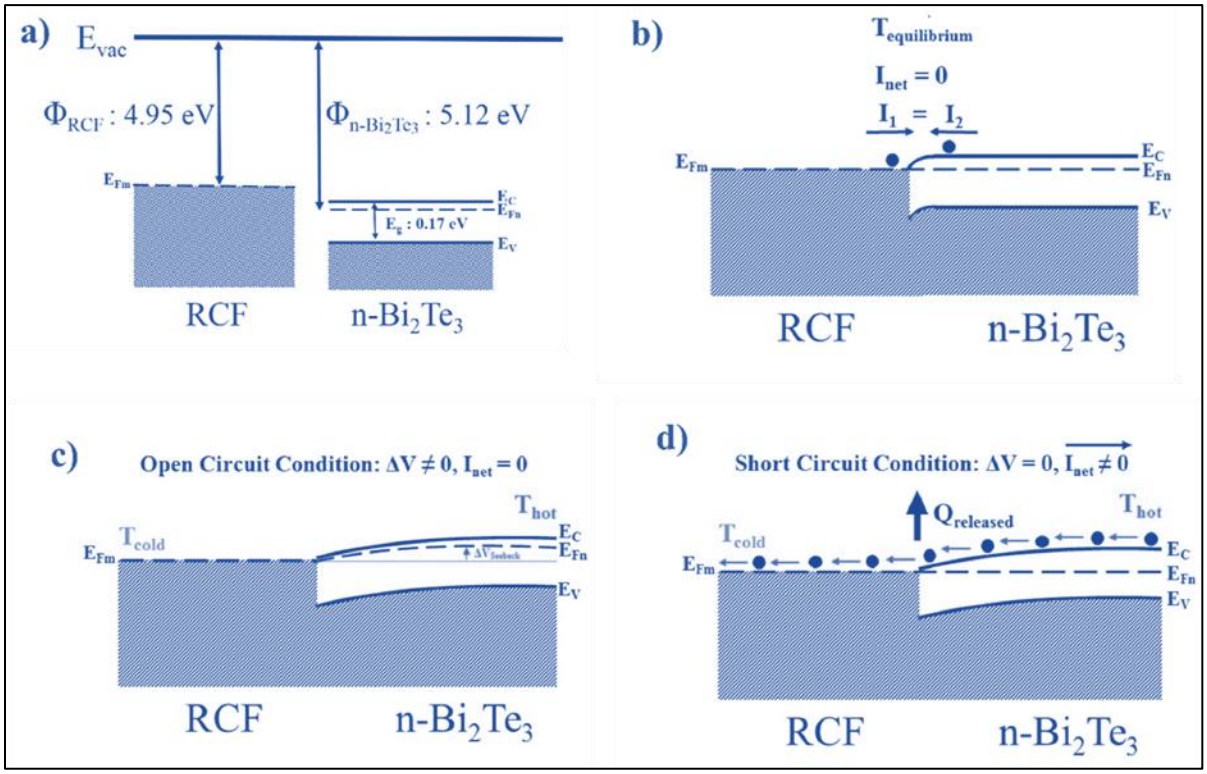

Figure 18: Schematic of the energy band diagram of (a) RCF and n-Bi_2Te_3 in isolation (b) RCF and n-Bi_2Te_3 in thermal equilibrium (c) RCF and n-Bi_2Te_3 subjected to temperature gradient in open circuit condition (d) RCF and n-Bi_2Te_3 subjected to temperature gradient in closed circuit condition.

Consequently, the Fermi level changes as a function of temperature according to Eq (6), as shown below [67].

$$(E_C - E_F) = kTln\frac{N_C}{N_d - N_a} \qquad (6)$$

Whereby (E_C-E_F) is the difference in the energy level of Fermi level and conduction band edge, k is the Boltzmann constant in $eV.K^{-1}$, T is the temperature in Kelvin, N_C is the effective density of

states in the conduction band, N_d is electron concentration in the conduction band, and N_a is hole concentration in the valence band.

As per equation (6), the Fermi level in n-Bi_2Te_3 moves away from the EC with an increase in temperature and vice versa, owing to the temperature gradient. This shift in the Fermi level of n-Bi_2Te_3 concerning the Fermi level of RCF leads to the observation of a Seebeck voltage in an open circuit condition. As an extension of our current study, we would also like to postulate the possibility of a cross-plane thermoelectric generator (TEG) from RCF/n-Bi_2Te_3 heterostructure thermoelectric composite. As the work function of n-Bi_2Te_3 is higher than the work function of RCF, an ohmic metal-semiconductor contact is established [68]. From the charge carrier transport perspective, an ohmic contact allows bi-directional movement of charge carriers (electrons in this case) depending on the direction of the thermal gradient, which allows extraction of thermoelectric generated current in a closed-circuit condition as depicted in Figure 18 (d). Our preliminary investigation revealed that a current density in the range of 25 nA/cm^2 to 162 nA/cm^2 could be obtained from this cross-plane RCF/n-Bi_2Te_3 heterostructure thermoelectric composite configuration. To the best of our knowledge, no studies have been reported in the literature thus far pertaining to the proof-of-concept of RCF/n-Bi_2Te_3 cross-plane TEG, as demonstrated in this study. However, the obtained current density is low and significant improvements are required to enhance further the current density for practical utilization in sub-watt power generation for various applications. Therefore, as a continuation of this finding, we are undertaking a systematic investigation to address the performance limiting factors of RCF/n-Bi_2Te_3 cross-plane TEG. The outcomes will be reported in future publications.

Comparison of power factor enhancement with literature review

Table 5 presents a comparison of various methods employed to enhance the power factor, including material doping, morphology modification, thickness modification, and thermal annealing. According to Cai et al., the annealing of Bi_2Te_3 films at 400 ^oC for 60 mins has enhanced the power factor by 1,090 %, which is the highest even compared with the power factor enhancement of other recent studies [69]. Notably, our study demonstrates an even more significant power enhancement of 4,021% by annealing the Bi2Te3/RCF at 350 oC for 120 minutes (2 hours), which is approximately four times greater than the improvement reported by Cai et al. These findings suggest that the annealing duration is crucial in augmenting the power factor. Consequently, future investigations in this field should consider adjusting the annealing time to enhance the power factor further.

Table 5: Comparison of the power factor enhancement of this study with literature review.

Thermoelectric materials	**Enhancement in Power Factor (%)**
Annealed Bi_2Te_3/RCF of 350 ^oC for 120 minutes (This study)	4,021
Controlled nanaowire interfaced and Al-doped ZnO [70]	53
Rapid thermal annealing (RTA) at 900 ^oC for 20 s after thermal activation annealing at 600-650 ^oC for 2 min of β-$FeSi_2$ doped Si nanostructure [39]	200
Reduced thickness of ultrathin Bi_2Te_3 film [71]	868
Zn-doped Bi_2Te_3 [72]	121
Co-doped Bi_2Te_3 [73]	47
Cu-doped Bi_2Te_3 [74]	~99
Annealing of Bi_2Te_3 films at 400 ^oC for 60 mins [69]	1,090
Annealing of nanostructured $Bi_{0.7}Sb_{1.3}Te_3$ film at 200 ^oC for 30 mins [75]	300
PbTe doping and annealing of Bi_2Te_3 at 300 ^oC for 60 mins [76]	~400

Conclusion

This investigation examines the impact of annealing conditions, specifically temperature and duration, on the thermoelectric performance, carrier transport, morphology, structural integrity,

and thermal stability characteristics of annealed RCF-Bi_2Te_3 composites. Some of the key findings can be summarized as:

a. The optimum annealing profile for annealing temperature and time for RCF-Bi_2Te_3 composites is 350 °C and 2 hours, respectively, which yielded an optimal power factor of 7.83 $\mu WK^{-2}m^{-1}$.
b. The annealed RCF-Bi_2Te_3 composites exhibited almost 4000% improvement in their power factor compared to the non-annealed (0.19 $\mu WK^{-2}m^{-1}$) counterparts at optimum annealing temperature and time.
c. Nucleation and grain growth enlargement during annealing have substantially improved the charge carrier transport and structural properties of the Bi_2Te_3 particles, which improved the thermoelectric performance of the annealed RCF-Bi_2Te_3 composites tremendously.
d. It is observed that annealing at higher temperatures and longer duration led to the evaporation of tellurium, which reduced the thermoelectric performance of the RCF-Bi_2Te_3 composites.
e. It can be also elucidated that RCF and n-Bi_2Te_3 can be readily adapted as a cross-plane thermoelectric generator (TEG) due to favourable heterojunction band alignment.

The present study establishes a foundation for exploring diverse practical avenues for re-utilizing RCF (reinforced carbon fiber) in thermoelectric applications. Furthermore, it is advisable to examine the impact of annealing temperature and duration on thermoelectric materials in future investigations to attain optimal enhancement of thermoelectric performance through thermal annealing. Additionally, future research endeavors in the field of thermoelectric materials development could encompass the synthesis of these materials under optimized conditions, along

with the introduction of nanomaterial doping prior to thermal annealing, thereby warranting further investigation.

Acknowledgments

The authors thank the Ministry of Education, Malaysia, for funding through the Fundamental Research Grant Scheme (FRGS/1/2020/TK0/SYUC/01/3). The authors would also like to acknowledge the University of Nottingham Malaysia and the Centre of Research Instrumentation and Management (CRIM), Universiti Kebangsaan Malaysia, for their technical support in material characterization services. Author Contribution . Priyanka R. Jagadish: Conceptualization, Methodology, Validation, Formal Analysis, Investigation, Data Curation, Project Administration, Writing - Original Draft, Visualization. Mohammad Khalid: Resources, Writing - Review & Editing, Supervision, Project Administration, Resources, Funding Acquisition. N.M Mubarak & Rashmi Walvekar: Resources, Funding Acquisition, Project Administration. Puvaneswaran Chelvanathan & Wong Weng Pin: Formal Analysis, Writing - Original Draft, Visualization. Lau Phei Li & Andy Chan: Supervision, Resources. Declaration of Competing Interest. The authors declare that they have no known competing financial interests or personal relationships that could have appeared to influence the work reported in this paper.

References

[1] D.J. Kwon, J.H. Kim, S.M. Park, I.J. Kwon, K.L. DeVries, J.M. Park, Damage sensing, mechanical and interfacial properties of resins suitable for new CFRP rope for elevator applications, Compos B Eng. 157 (2019) 259–265. https://doi.org/10.1016/j.compositesb.2018.08.049.

[2] D. Quan, F. Bologna, G. Scarselli, A. Ivankovic, N. Murphy, Interlaminar fracture toughness of aerospace-grade carbon fibre reinforced plastics interleaved with thermoplastic veils, Compos Part A Appl Sci Manuf. 128 (2020). https://doi.org/10.1016/j.compositesa.2019.105642.

[3] I. Ribeiro, J. Kaufmann, U. Götze, P. Peças, E. Henriques, Fibre reinforced polymers in the sports industry–Life Cycle Engineering methodology applied to a snowboard using anisotropic layer design, International Journal of Sustainable Engineering. 12 (2019) 201–211. https://doi.org/10.1080/19397038.2018.1508318.

[4] V.P. McConnell, Decoding the ‘stealth factor’ in global carbon fibre supply and demand, Reinforced Plastics. 52 (2008) 18–23. https://doi.org/https://doi.org/10.1016/S0034-3617(08)70273-X.

[5] S. Das, Sujit; Warren, Josh; West, Devin; Schexnayder, Global Carbon Fiber Composites Supply Chain Competitiveness Analysis, Tennessee, 2016.

[6] A. Lefeuvre, S. Garnier, L. Jacquemin, B. Pillain, G. Sonnemann, Anticipating in-use stocks of carbon fibre reinforced polymers and related waste generated by the wind power sector until 2050, Resour Conserv Recycl. 141 (2019) 30–39. https://doi.org/10.1016/j.resconrec.2018.10.008.

[7] Thermoelectric Generators Market to Hit USD 1633.76 Million, (n.d.). https://www.globenewswire.com/en/news-release/2023/05/05/2662591/0/en/Thermoelectric-Generators-Market-to-Hit-USD-1633-76-Million-by-2030-Driven-by-Growing-Demand-for-Reliable-and-Uninterrupted-Power-Supply-Research-by-SNS-Insider.html (accessed June 2, 2023).

[8] A. Isa, N. Nosbi, M. Che Ismail, H. Md Akil, W.F.F. Wan Ali, M.F. Omar, A Review on Recycling of Carbon Fibres: Methods to Reinforce and Expected Fibre Composite Degradations, Materials. 15 (2022). https://doi.org/10.3390/ma15144991.

[9] E. Pakdel, S. Kashi, R. Varley, X. Wang, Recent progress in recycling carbon fibre reinforced composites and dry carbon fibre wastes, Resour Conserv Recycl. 166 (2021). https://doi.org/10.1016/j.resconrec.2020.105340.

[10] F. Meng, J. McKechnie, S.J. Pickering, An assessment of financial viability of recycled carbon fibre in automotive applications, Compos Part A Appl Sci Manuf. 109 (2018) 207–220. https://doi.org/10.1016/j.compositesa.2018.03.011.

[11] M. Boulanghien, M. R'Mili, G. Bernhart, F. Berthet, Y. Soudais, Mechanical Characterization of Carbon Fibres Recycled by Steam Thermolysis: A Statistical Approach, Advances in Materials Science and Engineering. 2018 (2018). https://doi.org/10.1155/2018/8630232.

[12] G. Cai, M. Wada, I. Ohsawa, S. Kitaoka, J. Takahashi, Tensile properties of recycled carbon fibers subjected to superheated steam treatment under various conditions, Compos Part A Appl Sci Manuf. 133 (2020) 105869. https://doi.org/10.1016/j.compositesa.2020.105869.

[13] F. Fernandez, Andrea; Lopez, Claudio; Gonzalez, Carlos; Lopez, Characterization of Carbon Fibers Recovered by Pyrolysis of Cured Prepregs and Their Reuse in New Composites, in: Recent Developments in the Field of Carbon Fibers, IntechOpen, 2018: pp. 104–120.

[14] J. Palmer, L. Savage, O.R. Ghita, K.E. Evans, Sheet moulding compound (SMC) from carbon fibre recyclate, Compos Part A Appl Sci Manuf. 41 (2010) 1232–1237. https://doi.org/10.1016/j.compositesa.2010.05.005.

[15] K.H. Wong, S.J. Pickering, C.D. Rudd, Recycled carbon fibre reinforced polymer composite for electromagnetic interference shielding, Compos Part A Appl Sci Manuf. 41 (2010) 693–702. https://doi.org/10.1016/j.compositesa.2010.01.012.

[16] S. Schlichter, T. Gries, NOVEL PERSPECTIVES IN USE OF RECYCLED CARBON FIBRES – HEATING , SHIELDING AND MAINTENANCE, 1 (2019) 2–5.

[17] M. Kim, D.H. Sung, K. Kong, N. Kim, B.J. Kim, H.W. Park, Y. Bin Park, M. Jung, S.H. Lee, S.G. Kim, Characterization of resistive heating and thermoelectric behavior of discontinuous carbon fiber-epoxy composites, Compos B Eng. 90 (2016) 37–44. https://doi.org/10.1016/j.compositesb.2015.11.037.

[18] D.H. Sung, G.H. Kang, K. Kong, M. Kim, H.W. Park, Y. Bin Park, Characterization of thermoelectric properties of multifunctional multiscale composites and fiber-reinforced composites for thermal energy harvesting, Compos B Eng. 92 (2016) 202–209. https://doi.org/10.1016/j.compositesb.2016.02.050.

[19] D. Rowe, Introduction, in: CRC Handbook of Thermoelectrics, CRC Press, Boca Raton, 1995. https://doi.org/doi:10.1201/9781420049718.ch1.

[20] P.A. Finn, C. Asker, K. Wan, E. Bilotti, O. Fenwick, C.B. Nielsen, Thermoelectric Materials: Current Status and Future Challenges, Frontiers in Electronic Materials. 1 (2021). https://doi.org/10.3389/femat.2021.677845.

[21] R. Venkatasubramanian, E. Siivola, T. Colpitts, B. O'quinn, Thin-film thermoelectric devices with high room-temperature figures of merit, Nature. (2001) 597–602.

[22] J. Wei, L. Yang, Z. Ma, P. Song, M. Zhang, J. Ma, F. Yang, X. Wang, Review of current high-ZT thermoelectric materials, J Mater Sci. 55 (2020) 12642–12704. https://doi.org/10.1007/s10853-020-04949-0.

[23] S. Li, J. Pei, D. Liu, L. Bao, J.F. Li, H. Wu, L. Li, Fabrication and characterization of thermoelectric power generators with segmented legs synthesized by one-step spark plasma sintering, Energy. 113 (2016) 35–43. https://doi.org/10.1016/j.energy.2016.07.034.

[24] H. Song, K. Cai, Preparation and properties of PEDOT:PSS/Te nanorod composite films for flexible thermoelectric power generator, Energy. 125 (2017) 519–525. https://doi.org/10.1016/j.energy.2017.01.037.

[25] Y. Guo, J. Mu, C. Hou, H. Wang, Q. Zhang, Y. Li, Flexible and thermostable thermoelectric devices based on large-area and porous all-graphene films, Carbon N Y. 107 (2016) 146–153. https://doi.org/10.1016/j.carbon.2016.05.063.

[26] W. Peng, Huisheng;Sun, Xuemei;XinFang, Energy Harvesting Based on Polymer, in: S. Tian (Ed.), Polymer Materials for Energy and Electronic Applications, Elsevier, 2017: pp. 151–196.

[27] P.R. Jagadish, M. Khalid, L.P. Li, M.T. Hajibeigy, N. Amin, R. Walvekar, A. Chan, Cost effective thermoelectric composites from recycled carbon fibre: From waste to energy, J Clean Prod. 195 (2018). https://doi.org/10.1016/j.jclepro.2018.05.238.

[28] P.R. Jagadish, M. Khalid, N. Amin, L.P. Li, A. Chan, Process optimization for n-type Bi<inf>2</inf>Te<inf>3</inf> films electrodeposited on flexible recycled carbon fibre

using response surface methodology, J Mater Sci. 52 (2017). https://doi.org/10.1007/s10853-017-1284-2.

[29] P.R. Jagadish, L.P. Li, A. Chan, M. Khalid, Effect of Annealing on Virgin and Recycled Carbon Fiber Electrochemically Deposited with N-type Bismuth Telluride and Bismuth Sulfide, Materials and Manufacturing Processes. 31 (2016) 1223–1231. https://doi.org/10.1080/10426914.2015.1090590.

[30] P.R. Jagadish, M. Khalid, L.P. Li, N. Amin, R. Walvekar, A. Chan, Effect of graphene doping on the charge carrier and thermoelectric properties of RCF-Bi2S3 composites, AIP Conf Proc. 2137 (2019). https://doi.org/10.1063/1.5120980.

[31] P. Jagadish, M. Khalid, N. Amin, M.T. Hajibeigy, L.P. Li, A. Numan, N.M. Mubarak, R. Walvekar, A. Chan, Recycled carbon fibre/Bi2Te3 and Bi2S3 hybrid composite doped with MWCNTs for thermoelectric applications, Compos B Eng. 175 (2019). https://doi.org/10.1016/j.compositesb.2019.107085.

[32] Z. Wu, E. Mu, Z. Che, Y. Liu, F. Sun, X. Wang, Z. Hu, Nanoporous (00l)-oriented Bi2Te3 nanoplate film for improved thermoelectric performance, J Alloys Compd. 828 (2020) 154239. https://doi.org/10.1016/j.jallcom.2020.154239.

[33] M. Kim, T. Oh, J. Kim, M.-Y. Min-Young, T.-S. Tae-Sung, J.-S. Jin-Sang, Annealing Behavior of Bi2Te3 Thermoelectric Semiconductor Electrodeposited for Nanowire Applications, Journal of the Korean Physical Society. 50 (2007) 670. https://doi.org/10.3938/jkps.50.670.

[34] S. Elyamny, B. Kashyout, Preparation and characterization of the nanostructured bismuth telluride thin films deposited by thermal evaporation technique, Mater Today Proc. 8 (2019) 680–689. https://doi.org/10.1016/j.matpr.2019.02.068.

[35] D.D. Le, T.S. Ngo, S.K. Hong, Effect of in situ annealing on the structural properties of Bi2Te3 films grown on (0 0 0 1) sapphire, J Cryst Growth. 525 (2019). https://doi.org/10.1016/j.jcrysgro.2019.125191.

[36] M. Sun, G. Tang, B. Huang, Z. Chen, Y.-J. Zhao, H. Wang, Z. Zhao, D. Chen, Q. Qian, Z. Yang, Tailoring microstructure and electrical transportation through tensile stress in Bi2Te3 thermoelectric fibers, Journal of Materiomics. (2020). https://doi.org/10.1016/j.jmat.2020.02.004.

[37] Z. He, Y.X. Chen, Z. Zheng, F. Li, G. Liang, J. Luo, P. Fan, Enhancement of thermoelectric performance of N-type Bi2Te3 based thin films via in situ annealing during magnetron sputtering, Ceram Int. (2020). https://doi.org/10.1016/j.ceramint.2020.02.117.

[38] P. Jagadish, DEVELOPMENT AND CHARACTERIZATION OF RECYCLED CARBON FIBRE BASED FILMS/COMPOSITES FOR THERMOELECTRIC APPLICATIONS, n.d.

[39] S. Sakane, T. Ishibe, T. Taniguchi, N. Naruse, Y. Mera, T. Fujita, M.M. Alam, K. Sawano, N. Mori, Y. Nakamura, Thermoelectric power factor enhancement based on carrier transport physics in ultimately phonon-controlled Si nanostructures, 2019.

[40] B.A. Hasan, I.H. Shallal, Structural and Optical Properties of SnS Thin Films, Journal of Nanotechnology and Advanced Materials. 2 (2014) 43–49. https://doi.org/10.1080/17458080.2013.788226.

[41] E. Yücel, Y. Yücel, Fabrication and characterization of Sr-doped PbS thin films grown by CBD, Ceram Int. 43 (2017) 407–413. https://doi.org/10.1016/j.ceramint.2016.09.173.

[42] E. Yücel, Y. Yücel, Effect of doping concentration on the structural, morphological and optical properties of Ca-doped PbS thin films grown by CBD, Optik - International Journal for Light and Electron Optics. 142 (2017) 82–89. https://doi.org/https://doi.org/10.1016/j.ijleo.2017.04.104.

[43] C. Sudarshan, S. Jayakumar, K. Vaideki, S. Nandy, C. Sudakar, Structural, electrical, optical and thermoelectric properties of e-beam evaporated Bi-rich Bi 2 Te 3 thin films, Thin Solid Films. 672 (2019) 165–175. https://doi.org/10.1016/j.tsf.2019.01.010.

[44] S. Han, D.D.L. Chung, Carbon fiber polymer-matrix structural composites exhibiting greatly enhanced through-thickness thermoelectric figure of merit, Compos Part A Appl Sci Manuf. 48 (2013) 162–170. https://doi.org/10.1016/j.compositesa.2013.01.008.

[45] L. Shuai, L. Fei, Z. Xiaoqi, B. Yu, M. Dayan, M. Fei, X. Kewei, Elemental Ratio Controlled Semiconductor Type of Bismuth Telluride Alloy Thin Films, Rare Metal Materials and Engineering. 44 (2015) 3041–3044. https://doi.org/10.1016/S1875-5372(16)60047-4.

[46] M.M. Rashid, K.H. Cho, G.-S. Chung, Rapid thermal annealing effects on the microstructure and the thermoelectric properties of electrodeposited Bi2Te3 film, Appl Surf Sci. 279 (2013) 23–30. https://doi.org/10.1016/j.apsusc.2013.03.112.

[47] X. Wang, H. He, N. Wang, L. Miao, Effects of annealing temperature on thermoelectric properties of Bi 2 Te 3 films prepared by co-sputtering, Appl Surf Sci. 276 (2013) 539–542. https://doi.org/10.1016/j.apsusc.2013.03.130.

[48] S. Jeon, M. Oh, H. Jeon, S. Hyun, H. Lee, Effects of post-annealing on thermoelectric properties of bismuth–tellurium thin films deposited by co-sputtering, Microelectron Eng. 88 (2011) 541–544. https://doi.org/10.1016/j.mee.2010.06.036.

[49] W.S. Liu, Q. Zhang, Y. Lan, S. Chen, X. Yan, Q. Zhang, H. Wang, D. Wang, G. Chen, Z. Ren, Thermoelectric property studies on Cu-doped n-type Cu xBi 2Te 2.7Se 0.3 nanocomposites, Adv Energy Mater. 1 (2011) 577–587. https://doi.org/10.1002/aenm.201100149.

[50] D. Kong, W. Zhu, Z. Guo, Y. Deng, High-performance flexible Bi2Te3 films based wearable thermoelectric generator for energy harvesting, Energy. 175 (2019) 292–299. https://doi.org/10.1016/j.energy.2019.03.060.

[51] K. Singkaselit, A. Sakulkalavek, R. Sakdanuphab, Effects of annealing temperature on the structural, mechanical and electrical properties of flexible bismuth telluride thin films prepared by high-pressure RF magnetron sputtering, Advances in Natural Sciences: Nanoscience and Nanotechnology. 8 (2017). https://doi.org/10.1088/2043-6254/aa7222.

[52] S. Liu, F. Liu, X.Q. Zhu, Y. Bai, D.Y. Ma, F. Ma, K.W. Xu, Limited grain growth in multilayered Bi/Te thin films and the influence on the thermal and electrical conductivity, Vacuum. 127 (2016) 88–95. https://doi.org/10.1016/j.vacuum.2016.02.013.

[53] Z. Zeng, P. Yang, Z. Hu, Temperature and size effects on electrical properties and thermoelectric power of Bismuth Telluride thin films deposited by co-sputtering, Appl Surf Sci. 268 (2013) 472–476. https://doi.org/10.1016/j.apsusc.2012.12.134.

[54] H. Huang, W. Luan, S. Tu, Influence of annealing on thermoelectric properties of bismuth telluride films grown via radio frequency magnetron sputtering, Thin Solid Films. 517 (2009) 3731–3734. https://doi.org/10.1016/j.tsf.2009.01.015.

[55] R. Mori, Y. Mayuzumi, M. Yamaguchi, A. Kobayashi, Y. Seki, M. Takashiri, Improved thermoelectric properties of solvothermally synthesized Bi2Te3 nanoplate films with homogeneous interconnections using Bi2Te3 electrodeposited layers, J Alloys Compd. 818 (2020) 152901. https://doi.org/10.1016/j.jallcom.2019.152901.

[56] J. Lee, J. Kim, W. Moon, A. Berger, J. Lee, Enhanced Seebeck Coe ffi cients of Thermoelectric Bi 2 Te 3 Nanowires as a Result of an Optimized Annealing Process, (2012) 19512–19516.

[57] D.-H. Kim, G.-H. Lee, Effect of rapid thermal annealing on thermoelectric properties of bismuth telluride films grown by co-sputtering, Materials Science and Engineering: B. 131 (2006) 106–110. https://doi.org/10.1016/j.mseb.2006.03.034.

[58] I.J. Ohsugi, D. Tokunaga, M. Kato, S. Yoneda, Y. Isoda, Dissociation and sublimation of tellurium from the thermoelectric tellurides, Materials Research Innovations. 19 (2015) S5-301-S5-303. https://doi.org/10.1179/1432891714Z.0000000001097.

[59] D. Zhao, J. Chen, Z. Ren, J. Chen, Q. Song, Q. Zhang, N. Chen, Y. Jiang, Thermoelectric transport and magnetoresistance of electrochemical deposited Bi2Te3 films at micrometer thickness, Ceram Int. 46 (2020) 3339–3344. https://doi.org/10.1016/j.ceramint.2019.10.043.

[60] J. Hamada, M. Takashiri, Structural changes in nanocrystalline Bi2Te3/Bi2Se3multilayer thin films caused by thermal annealing, J Cryst Growth. 468 (2017) 188–193. https://doi.org/10.1016/j.jcrysgro.2016.11.130.

[61] Y. Wang, W.-D. Liu, X.-L. Shi, M. Hong, L.-J. Wang, M. Li, H. Wang, J. Zou, Z.-G. Chen, Enhanced thermoelectric properties of nanostructured n-type Bi2Te3 by suppressing Te vacancy through non-equilibrium fast reaction, Chemical Engineering Journal. (2019) 123513. https://doi.org/10.1016/j.cej.2019.123513.

[62] H. An, M. Pusko, D. Chun, S. Park, J. Moon, In-situ synthesis of flexible hybrid composite films for improved thermoelectric performance, Chemical Engineering Journal. 357 (2019) 547–558. https://doi.org/10.1016/j.cej.2018.09.200.

[63] S. Han, D.D.L. Chung, Through-thickness thermoelectric power of a carbon fiber/epoxy composite and decoupled contributions from a lamina and an interlaminar interface, Carbon N Y. 52 (2013) 30–39. https://doi.org/10.1016/j.carbon.2012.08.071.

[64] X. Cai, S. Hou, H. Wu, Z. Lv, Y. Fu, D. Wang, C. Zhang, H. Kafafy, Z. Chu, D. Zou, All-carbon electrode-based fiber-shaped dye-sensitized solar cells, Physical Chemistry Chemical Physics. 14 (2012) 125–130. https://doi.org/10.1039/c1cp22613d.

[65] B. Ryu, Work function of bismuth telluride: First-principles approach, Journal of the Korean Physical Society. 72 (2018) 122–128. https://doi.org/10.3938/jkps.72.122.

[66] S.M. Sze, Semiconductor Devices: Physics and Technology, Second Edi, Wiley, 2002.

[67] S. Wang, Fundamentals of Semiconductor Theory and Device Physics, Prentice-H, Prentice-Hall, Inc, 1989.

[68] S.K. Streetman, Ben G.; Banerjee, Solid State Electronic Devices, Sixth Edit, Pearson Education Inc, New Jersey, 2002.

[69] Z.K. Cai, P. Fan, Z.H. Zheng, P.J. Liu, T.B. Chen, X.M. Cai, J.T. Luo, G.X. Liang, D.P. Zhang, Thermoelectric properties and micro-structure characteristics of annealed N-type bismuth telluride thin film, Appl Surf Sci. 280 (2013) 225–228. https://doi.org/10.1016/j.apsusc.2013.04.138.

[70] T. Ishibe, A. Tomeda, K. Watanabe, Y. Kamakura, N. Mori, N. Naruse, Y. Mera, Y. Yamashita, Y. Nakamura, Methodology of Thermoelectric Power Factor Enhancement by Controlling Nanowire Interface, ACS Appl Mater Interfaces. 10 (2018) 37709–37716. https://doi.org/10.1021/acsami.8b13528.

[71] M. Ahmad, K. Agarwal, B.R. Mehta, An anomalously high Seebeck coefficient and power factor in ultrathin Bi2Te3film: Spin-orbit interaction, J Appl Phys. 128 (2020). https://doi.org/10.1063/5.0007440.

[72] A. Singh, P. Shahi, A.K. Ghosh, J.G. Cheng, S. Chatterjee, Enhancement in power factor due to anti-correlation between electrical conductivity and thermoelectric power and induced magnetic ordering in high mobility Zn doped Bi2Te3 topological insulator, J Alloys Compd. 731 (2018) 297–302. https://doi.org/10.1016/j.jallcom.2017.10.039.

[73] P. Singha, S. Das, V.A. Kulbashinskii, V.G. Kytin, S. Chakravarty, A.K. Deb, S. Bandyopadhyay, A. Banerjee, Enhancement of electron mobility and thermoelectric power factor of cobalt-doped n-type Bi2Te3, Int J Energy Res. 46 (2022) 17029–17042. https://doi.org/10.1002/er.8366.

[74] J. Cha, C. Zhou, S.P. Cho, S.H. Park, I. Chung, Ultrahigh Power Factor and Electron Mobility in n-Type Bi2Te3- x%Cu Stabilized under Excess Te Condition, ACS Appl Mater Interfaces. 11 (2019) 30999–31008. https://doi.org/10.1021/acsami.9b10394.

[75] P.P. Murmu, J. Kennedy, S. Suman, S. V. Chong, J. Leveneur, J. Storey, S. Rubanov, G. Ramanath, Multifold improvement of thermoelectric power factor by tuning bismuth and antimony in nanostructured n-type bismuth antimony telluride thin films, Mater Des. 163 (2019). https://doi.org/10.1016/j.matdes.2018.107549.

[76] S. Liang, H. Zhu, X. Ge, S. Yue, Enhanced power factor of Bi0.5Sb1.5Te3 thin films via PbTe incorporating and annealing, Surfaces and Interfaces. 24 (2021). https://doi.org/10.1016/j.surfin.2021.101099.